

1 **Influences of Recent Particle Formation on Southern Ocean Aerosol Variability and**
2 **Low Cloud Properties**
3

4 **Isabel L. McCoy¹, Christopher S. Bretherton¹, Robert Wood¹, Cynthia H. Twohy², Andrew**
5 **Gettelman³, Charles G. Bardeen³, and Darin W. Toohey⁴**

6
7 ¹ Atmospheric Sciences, University of Washington, Seattle, WA, USA, ² Northwest Research
8 Associates, Redmond, WA, USA, ³ National Center for Atmospheric Research, Boulder, CO,
9 USA, ⁴ Atmospheric and Oceanic Sciences, University of Colorado, Boulder, CO, USA.

10
11 Corresponding author: Isabel L. McCoy (imccoy@ucar.edu)
12

13 **Key Points:**

- 14 • Summertime Southern Ocean free tropospheric aerosol number is dominated by Aitken
15 particles recently generated through synoptic uplift.
16 • Entrained Aitken aerosols buffer Southern Ocean boundary layer cloud condensation
17 nuclei and cloud droplets against precipitation removal.
18 • Southern Ocean cloud droplet number is too low in the CAM6 climate model due to
19 inadequate free tropospheric production of Aitken aerosols.
20

21 **Abstract**

22 Controls on pristine aerosol over the Southern Ocean (SO) are critical for constraining the
23 strength of global aerosol indirect forcing. Observations of summertime SO clouds and aerosols
24 in synoptically varied conditions during the 2018 SOCRATES aircraft campaign reveal novel
25 mechanisms influencing pristine aerosol-cloud interactions. The SO free troposphere (3-6 km) is
26 characterized by widespread, frequent new particle formation events contributing to much larger
27 concentrations ($\geq 1000 \text{ mg}^{-1}$) of condensation nuclei (diameters $> 0.01 \mu\text{m}$) than in typical sub-
28 tropical regions. Synoptic-scale uplift in warm conveyor belts and sub-polar vortices lifts marine
29 biogenic sulfur-containing gases to free-tropospheric environments favorable for generating
30 Aitken-mode aerosol particles (0.01-0.1 μm). Free-tropospheric Aitken particles subside into the
31 boundary layer, where they grow in size to dominate the sulfur-based cloud condensation nuclei
32 (CCN) driving SO cloud droplet number concentrations ($N_d \sim 60\text{-}100 \text{ cm}^{-3}$). Evidence is
33 presented for a hypothesized Aitken-buffering mechanism which maintains persistently high
34 summertime SO N_d against precipitation removal through CCN replenishment from activation
35 and growth of boundary layer Aitken particles. Nudged hindcasts from the Community
36 Atmosphere Model (CAM6) are found to underpredict Aitken and accumulation mode aerosols
37 and N_d , impacting summertime cloud brightness and aerosol-cloud interactions and indicating
38 incomplete representations of aerosol mechanisms associated with ocean biology.

39

40 **Plain Language Summary**

41 The remote Southern Ocean (SO) is a unique analogue to pre-industrial environments due to
42 limited continental and anthropogenic influences. Understanding how aerosols are produced in
43 this region and their influence on cloud droplet concentrations is vital for understanding how
44 much sunlight these clouds reflect to space, which affects ocean temperatures and global climate.
45 This is a key uncertainty in modeling past and future climate change due to anthropogenic
46 emissions of carbon dioxide and other pollutants. To understand this pristine environment, we
47 analyze novel observations of SO clouds and aerosols from a summertime aircraft campaign. We
48 present evidence for an aerosol production mechanism driven by synoptic storms and sourced
49 from emissions of ocean biology. This mechanism produces a reservoir of small aerosols above
50 cloud that subside into the marine boundary layer, where they grow into cloud-affecting sizes
51 and control cloud droplet number. In addition to acting as a source of boundary layer aerosol,
52 these small particles help SO clouds to resist precipitation depletion of cloud-affecting aerosol,
53 maintaining surprisingly high cloud droplet number concentrations that help to keep present-day
54 SO clouds persistently bright. This mechanism has important implications for understanding pre-
55 industrial and other pristine environments and their response to anthropogenic aerosol.

56 **1 Introduction**

57 The Southern Ocean (SO) is our closest present-day (PD) analog to the pre-industrial (PI)
58 state due to its pristine aerosol (Hamilton et al., 2014). It is also frequently cloudy, providing
59 ample opportunity for aerosol-cloud interactions (ACI) to take place. Understanding the climate
60 response to changes in anthropogenic aerosol (i.e. PI to PD states) will help to reduce the
61 uncertainty in global climate model (GCM) climate sensitivity and improve climate predictions
62 (Andreae et al., 2005; Forster, 2016). Aerosol-cloud interactions are the main contributor to
63 uncertainty in total radiative forcing (Bellouin et al., 2020). Poor understanding of PI aerosol

64 state is a leading driver of this uncertainty (Carslaw et al., 2013), making observations in pristine
65 locations that give us insight into PI aerosol and ACI doubly important. This was a central focus
66 of the 2018 Southern Ocean Clouds Radiation and Aerosol Transport Experimental Study
67 (SOCRATES) aircraft campaign that took place in the austral summer off the coast of Tasmania.

68 In the absence of continental influence (e.g. biomass burning and anthropogenic sources),
69 SO aerosol is composed of particles associated with ocean biology and, near the ocean surface,
70 sea spray. Aerosols fall into four modes: coarse (diameters $> 1 \mu\text{m}$), accumulation (0.1-1 μm),
71 Aitken (0.01-0.1 μm) and nucleation ($< 0.01 \mu\text{m}$) (Bates, 2002; Clarke et al., 1998; Seinfeld &
72 Pandis, 2016). Collectively, aerosols from all modes taken together are referred to as
73 condensation nuclei (CN). Accumulation mode aerosols are the main contributors to cloud
74 condensation nuclei (CCN) and are of central importance to ACI through their control of cloud
75 droplet number (N_d) and overall cloud albedo (Twomey, 1977). The role of giant CCN ($\geq 2 \mu\text{m}$)
76 (Jensen & Nugent, 2017) sampled during SOCRATES (McFarquhar et al., 2020) on SO
77 precipitation will be the topic of future papers. The number concentration of particles in the SO
78 is dominated by Aitken mode and small accumulation mode particles while the mass is
79 dominated by coarse mode particles (Ayers et al., 1997). Sea spray production mechanisms
80 contribute larger accumulation mode and coarse mode particles (diameters $\geq 0.2 \mu\text{m}$) (Bigg &
81 Leck, 2008; Fitzgerald, 1991; Grythe et al., 2014; Quinn et al., 2017) and dominate the
82 wintertime marine boundary layer (MBL) when biogenic sources are inactive. However, sea
83 spray aerosol is not the major contributor to summertime CCN (Modini et al., 2015; Prather et
84 al., 2013; Quinn et al., 2015) as these particles are estimated to contribute less than 30% of CCN
85 between 70°S and 80°N (Quinn et al., 2017).

86 Phytoplankton significantly influences the aerosol budget over the SO and other remote
87 marine regions during biologically active periods (e.g. spring and summer). Dimethylsulfonium
88 propionate (DMSP) is emitted by phytoplankton and subsequently cleaved into dimethyl sulfide
89 (DMS) and fluxed into the atmosphere. DMS oxidizes into methane sulfonic acid (MSA) and
90 sulfur dioxide (SO_2), which can further oxidize into sulfuric acid (H_2SO_4) (Ayers et al., 1997;
91 Fitzgerald, 1991; Quinn & Bates, 2011; Seinfeld & Pandis, 2016). SO_2 can also react in cloud
92 droplets through aqueous-phase oxidation and, after drop evaporation, create non-sea-salt sulfate
93 (nss- SO_4) particles which are extremely effective CCN (Charlson et al., 1987; Hobbs, 1971).
94 CCN also grow from coagulation of smaller Aitken or accumulation mode particles (Seinfeld &
95 Pandis, 2016) and from vapor deposition of DMS oxidation products (Ayers et al., 1997; Ayers
96 & Gillett, 2000; Ayers & Gras, 1991; Bates et al., 1998; Charlson et al., 1987) or organic gases
97 (Zheng et al., 2020) onto existing particles.

98 Aitken particles form mainly through homogeneous nucleation of precursor gases
99 (Seinfeld & Pandis, 2016), which, in the SO and other marine environments, are predominantly
100 H_2SO_4 and MSA (Ayers et al., 1997; Fitzgerald, 1991). Ions, organics, and other compounds can
101 also play a role in particle formation (Dunne et al., 2016; Gordon et al., 2017; Kerminen et al.,
102 2018). For gas to particle conversion to occur, precursor gases must be present and the total
103 aerosol surface area (SA, driven by coarse and accumulation mode sizes) must be low enough to
104 discourage vapor deposition on to preexisting particles ($\leq \sim 10 \mu\text{g cm}^{-3}$) (Clarke et al., 1998;
105 Covert et al., 1996). This low SA is likely to occur in the SO free troposphere (FT) (Clarke,
106 1993).

107 The majority of Aitken mode particles in marine regions are produced through gas to
108 particle conversion of DMS oxidation products in the FT and, after entraining or subsiding into
109 and growing in the MBL, they are the key source of CCN in the summertime SO. CCN (roughly

110 diameters $\leq 0.2 \mu\text{m}$) in the SO (Bigg, 2007; Bigg & Leck, 2008; Quinn et al., 2017), and
111 generally in remote marine environments between 70°S and 80°N (Quinn et al., 2017), are
112 dominated by nss-SO₄ in biologically active periods. These particles are often associated with
113 large scale meteorology that causes entrainment of recently formed Aitken particles from the FT
114 into the MBL (Quinn et al., 2017), which is thought to be the main source of aerosol number in
115 marine regions at low and middle latitudes (Kerminen et al., 2018). Variability in SO aerosol
116 concentrations is associated with frontal passages, rapidly bringing Aitken and nucleation mode
117 particles into the MBL from the FT ($40\text{-}70^\circ\text{S}$) (Bates et al., 1998; Covert et al., 1996). These
118 particles grow into CCN through gas condensation (Ayers et al., 1997; Ayers & Gillett, 2000;
119 Ayers & Gras, 1991; Bates et al., 1998; Charlson et al., 1987) and cloud processing (Sanchez et
120 al., 2021; Schmale et al., 2019), dominating aerosol size distributions between $20\text{-}70^\circ\text{S}$ (Covert
121 et al., 1996). Similar behavior is seen in the stormy, biologically active north Atlantic (Sanchez
122 et al., 2018; Zheng et al., 2020; Zheng et al., 2018). Faster descent over the SO relative to the
123 tropics reduces the amount of coagulation and growth that occurs (Clarke et al., 1998), which,
124 along with MBL residence time (Covert et al., 1996), affects how many aerosols grow to CCN
125 sizes.

126 Lack of positive correlations between aerosol surface area (SA) and concentrations of
127 nucleation mode particles in the SO MBL (Covert et al., 1996) suggest that new particle
128 formation is uncommon in the MBL (Bates et al., 1998) but instead occurs in the FT and
129 subsides into the MBL (Humphries et al., 2016; Sanchez et al., 2021; Schmale et al., 2019;
130 Williamson et al., 2019). This is consistent with the idea that short-term variability in MBL CCN
131 and CN is both limited and tied to FT processes (Raes, 1995). A global chemical transport model
132 estimation finds 43-65% of zonal mean CCN over the southern hemisphere summertime oceans
133 are from FT nucleated sulfate entrained and grown in the MBL (the dominant microphysical
134 pathway for DMS influencing southern hemisphere marine CCN) (Korhonen et al., 2008). More
135 recent modeling efforts have found the majority of spatiotemporal patterns in SO N_d are
136 explained by nss-SO₄ ($35\text{-}45^\circ\text{S}$) and organic matter in sea spray ($45\text{-}55^\circ\text{S}$), increasing the mean
137 summertime reflected shortwave by more than 10 W m^{-2} (D. T. McCoy et al., 2015).

138 Previously observed FT particle production over the SO has been associated with cloud
139 outflow (Clarke et al., 1998; Weber et al., 2001), a dominant particle formation mechanism
140 throughout the world that can involve a variety of cloud types (Kerminen et al., 2018) and
141 substantially influence aerosol concentrations (Twohy et al., 2002). Particle formation associated
142 with low cumulus clouds (Clarke et al., 1998) and a frontal cloud system (Weber et al., 2001)
143 have been observed over the SO simultaneous with H₂SO₄ vapors. Details have yet to be
144 quantified (Kerminen et al., 2018), but cloud outflow production broadly involves air masses rich
145 in precursor gases brought up through cloud and cleansed of accumulation and coarse mode
146 aerosol (reducing SA) through cloud droplet scavenging and precipitation processes.

147 After exiting cloud, precursor gases can oxidize and undergo gas to particle conversion
148 (low SA means pre-existing aerosols cannot scavenge these vapors (Weber et al., 2001)).
149 Depending on the exposure to liquid water, less water-soluble gases (e.g. DMS (Seinfeld &
150 Pandis, 2016)) better survive cloud and precipitation processing. Large eddy scale simulations of
151 gases processing through cloud before particle formation in cumulus outflow in the south east
152 Pacific (Kazil et al., 2011) suggest DMS is likely lofted through clouds before oxidizing into
153 precursor gases (e.g. MSA, SO₂ then H₂SO₄) after exposure to OH upon cloud exit.

154 Environments at higher altitudes over the SO are conducive to particle formation (Weber
155 et al., 2001): i) increased actinic flux from heightened upwelling and downwelling radiation

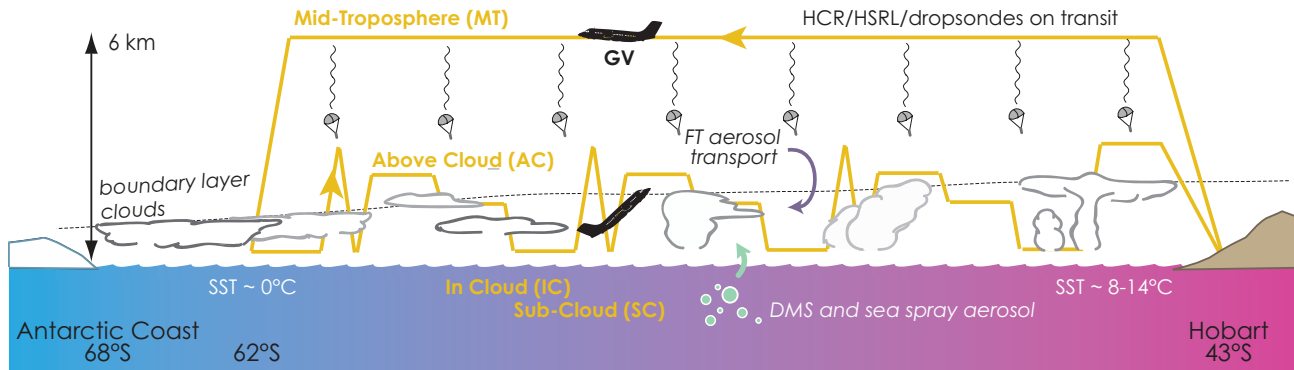
156 combined with heightened water vapor concentrations in cloud outflows can lead to increases in
157 OH and subsequent oxidation of DMS and its products, increasing precursor gas concentrations,
158 and ii) colder temperatures aloft increase the supersaturation of precursor gas concentrations,
159 increasing nucleation rates (Kirkby et al., 2011). Particle production rates at these altitudes are
160 incompletely explained by binary reactions (i.e. $\text{H}_2\text{SO}_4\text{-H}_2\text{O}$) (Weber et al., 2001) suggesting
161 other factors may also be involved (e.g. organics, ammonia, ions, etc.) (Dunne et al., 2016;
162 Gordon et al., 2017; Kirkby et al., 2011; Kürten et al., 2016).

163 SOCRATES was designed to expand our knowledge of the sources and sinks of aerosol
164 and the ACI in SO cyclone cold sectors ($45\text{-}62^\circ\text{S}$), a regime where Aitken aerosols are abundant
165 in the MBL (Covert et al., 1996; Quinn et al., 2017) and new particle formation occurs aloft
166 (Clarke et al., 1998; Weber et al., 2001). We detail widespread observations of recent particle
167 formation in the FT (3- 6 km) and the synoptic uplift mechanism that explains these frequently
168 occurring events (Section 3.1). Patterns of cloud, aerosol, and the resulting ACI are examined
169 and, building on earlier aerosol life-cycle and variability studies (Quinn et al., 2017; Raes, 1995),
170 a mechanism is hypothesized for N_d maintenance in SO clouds and pristine environments due to
171 entrained Aitken aerosol influence (Section 3.2). Global weather and climate models (GCMs)
172 simulate insufficiently bright low clouds in SO cold sectors (Bodas-Salcedo et al., 2016; Bodas-
173 Salcedo et al., 2012; Bodas-Salcedo et al., 2014; Williams et al., 2013), either due to excessive
174 glaciation of mixed-phase clouds or biases in CCN, N_d , and ACI (Bodas-Salcedo et al., 2019; I.
175 L. McCoy et al., 2020; Revell et al., 2019). Observational comparisons with SOCRATES nudged
176 GCMs highlight systematic biases that will help disentangle the cause of this radiative bias
177 (Section 3.3). We begin by describing our methodology, datasets, and models (Section 2) and
178 conclude with a discussion of the implications of this analysis and future steps (Section 4) as
179 well as a summary of our results (Section 5).

180 **2 Materials and Methods**

181 **2.1 Aircraft Sampling**

182 In the SOCRATES campaign (McFarquhar et al., 2020), the National Science Foundation
183 Gulfstream-V (GV) aircraft flew out of Hobart, Tasmania, over the SO. Fifteen flights (Figure
184 S1) were designed to sample low clouds in the cold sectors of cyclones. Each research flight
185 (RF) had a similar sampling strategy (Figure 1). The GV flew a high (~ 6 km altitude) survey leg
186 in the mid-troposphere (MT) into a region forecast to be dominated by low clouds, descending
187 after a southernmost latitude was reached ($\sim 60\text{-}62^\circ\text{S}$). After descending to an altitude above
188 cloud (~ 3 km), the GV returned to Hobart conducting repeated MBL flight modules. Each
189 module consisted of 10-minute level legs above cloud (AC), in cloud (IC), and sub cloud (SC) at
190 150 m above the sea surface, followed by sawtooth profiling through the MBL (Figure 1).
191 Module sampling was continued as long as operational constraints allowed after which the plane
192 climbed back above the MBL to return to Hobart. There were two exceptions to this method
193 during the campaign: RF11 and 15 had flight paths customized for targeting cumulus cloud tops
194 to sample mixed-phase microphysics. The limited observations obtained north of 45°S are
195 affected by proximity to Australia. Thus, our analysis focuses on the SO sampled between 45
196 and 62°S .



197

198 *Figure 1 Standard flight module for SOCRATES with identified sampling regions: mid-troposphere (MT), above cloud (AC), in*
 199 *cloud (IC), and sub-cloud (SC). A cloud radar (HCR), lidar (HSRL), and dropsondes were used to probe the underlying cloudy*
 200 *MBL on MT survey legs but are not explicitly utilized in this analysis (McFarquhar et al., 2020).*

201 The GV was equipped with a wide array of instruments (McFarquhar et al., 2020). The
 202 low-rate, 1 Hz flight, state, and microphysical data from the GV were used in this analysis
 203 (UCAR/NCAR, 2019). The cloud droplet number concentration (N_d) is from the cloud droplet
 204 probe (CDP). Aerosol number concentrations used in our analysis are taken from two
 205 instruments: a condensation nuclei counter (CN, aerosol diameters $\geq 0.011 \mu\text{m}$) and an ultra-high
 206 sensitivity aerosol spectrometer (UHSAS). Respectively, the instrument models used were a TSI-
 207 3760A condensation nucleus counter on a HIAPER modular inlet and a DMT UHSAS-A, S/N
 208 001. The UHSAS provides both size-resolved and integrated concentrations. The smallest size
 209 bins (diameters $< 0.1 \mu\text{m}$) are neglected due to sizing difficulties. Accumulation mode number
 210 concentrations are reported as UHSAS100 (0.1 – 1 μm diameter) throughout the paper,
 211 consistent with the expected size range for this mode. Size resolved number concentrations for
 212 coarse mode aerosol are from the CDP (2 – 50 μm diameter).

213 The surface area (SA) reported in this paper is computed from the coarse and
 214 accumulation mode size distributions (diameters between 0.1 and 50 μm). UHSAS reports
 215 essentially dry aerosol diameters except for the largest particles (Sanchez et al., 2021) while the
 216 CDP retains ambient diameters. Accumulation mode SA is adjusted for swelling associated with
 217 the environmental relative humidity before it is added to the coarse mode SA from the CDP. We
 218 use the growth factor reported for extinction coefficients, f_{grow} , in eq. 3 of Chand et al. (2012)
 219 scaled by 2/3 to account for SA growth (*personal communication Mike Reeves, NCAR*):

$$220 \quad SA_{\text{UHSAS}} = \pi D_{\text{UHSAS}}^2 f_{\text{grow}}^{2/3} \quad (1)$$

221 As in Chand et al. (2012), the values assumed in calculating f_{grow} are for sulfate aerosols, a
 222 somewhat smaller growth factor than for sea salt aerosols. This is a reasonable assumption
 223 because sulfate or sulfur-based aerosols were the most frequently observed throughout the
 224 campaign (Section 3.1.3).

225 All aerosol measurements are subject to screening by a cloud and rain mask based on the
 226 CDP and the two-dimensional optical array probe (2D-C). Aerosol observations were discarded
 227 when our empirically chosen thresholds were exceeded: liquid water content from the CDP \geq
 228 0.001 g m^{-3} or precipitation droplets from the 2D-C $\geq 0.1 \text{ L}^{-1}$. Samples were removed for 10
 229 seconds following detection of cloud or drizzle to avoid measurement contamination. Measured
 230 temperature and pressure are used to adjust aerosol concentrations to mg^{-1} from cm^{-3} to account

231 for volume changes at different levels in the atmosphere. Note that concentrations of mg^{-1} can be
232 converted to “ cm^{-3} at STP” by a factor of 1.25. Cumulative size distributions are calculated from
233 drizzle and cloud-screened aerosol number concentrations for CN, size resolved UHSAS, and
234 size resolved CDP.

235 Aerosol measurements behind a counterflow virtual impactor (CVI) (Noone et al., 1988;
236 Twohy et al., 1997) are used to interpret aerosol composition in two ways. First, Twohy et al.
237 (2021) use a scanning transmission electron microscope (STEM) and X-ray analysis of particles
238 impacted on formvar carbon grids for examining particles (diameters 0.1-1 μm) AC, IC, and SC
239 (Twohy et al., 2013). Specific examples for particles with diameters 0.1-0.5 μm are highlighted
240 here, see Twohy et al. (2021) for complete examination. Second, particle volatility estimates are
241 reconstructed for FT particles from comparing CVI heated CN (using a TSI-3010 condensation
242 nucleus counter, CN_{CVI}) and UHSAS100 (using a UHSAS-G, S/N 15 as in Kupc et al. (2018),
243 $\text{UHSAS100}_{\text{CVI}}$) measurements to un-heated CN and UHSAS100 measurements. Specifics of the
244 CVI set up for SOCRATES that allowed for this volatility analysis are detailed in supplementary
245 text S1. Particles are considered “volatilized” in this arrangement when their diameter is reduced
246 to below the detection limit for CN_{CVI} (0.011 μm) or $\text{UHSAS100}_{\text{CVI}}$ (0.1 μm) but they are likely
247 not completely evaporated.

248 Observations from the 2015 Cloud System Evolution in the Trades (CSET) campaign
249 (Albrecht et al., 2019) in the north east Pacific (NEP) provide a subtropical comparison for
250 SOCRATES. This comparison is modeled after Clarke et al. (1998) who used a similar tropical
251 comparison to establish the uniqueness of the SO. CSET sampled the stratocumulus to trade
252 cumulus transition between California and Hawaii using a modular strategy similar to
253 SOCRATES. Observations east of 130°W are continentally influenced and thus excluded from
254 this analysis. The GV during CSET was equipped with comparable wing-mounted
255 instrumentation including the CN, UHSAS, CDP, and 2D-C (UCAR/NCAR, 2017). The same
256 data screening and analysis methodology is applied to both campaigns.

257 Two kinds of binning composite methods are used in this paper. The first is a temporal by
258 altitude composite where median values are computed for observations from each flight binned
259 by 2 min in duration and 50 m in altitude. This is used for the majority of comparisons including
260 N_d versus UHSAS100 matches for interpreting ACI. The second is a distance by altitude
261 composite for describing regional characteristics. CSET and SOCRATES flight paths
262 approximately fall along common distance axes: a diagonal line between the coast of California
263 and Hawaii (CSET) (Bretherton et al., 2019) and a roughly north-south line between Hobart,
264 Tasmania and the coast of Antarctica (SOCRATES) (Figure S1). Median values are computed in
265 500 m altitude layers and 1.5° along the appropriate axis. Only bins with at least ten 1 Hz flight
266 observations are considered for both composite methods and aerosol samples are subject to the
267 same precipitation and cloud screening as described above. Individual distance by altitude flight
268 composites are averaged together to develop a mean campaign composite as in Bretherton et al.
269 (2019). Note that all correlation coefficients and p -values in this study are for Pearson
270 correlations, significance is assumed at 95% confidence, and R^2 is the variance explained.

271 **2.2 Air-mass Back Trajectories**

272 Interpreting SOCRATES aerosol observations requires knowledge of their air mass
273 histories. The Hybrid Single Particle Lagrangian Integrated Trajectory (HYSPLIT) model (Stein
274 et al., 2015) helps to provide this context. HYSPLIT back trajectories were based on Global Data
275 Assimilation System (GDAS) meteorology on a 0.5° by 0.5° grid. Seventy-two hour back-

276 trajectories were calculated for each 10-minute flight segment initialized with the aircraft
277 altitude, latitude, and longitude at the mean segment time.

278 **2.3 Nudged Global Climate Model Simulations**

279 A goal of both SOCRATES and CSET was to use observations to evaluate the fidelity of
280 current GCMs. One method is to compare campaign observations with reanalysis-nudged
281 hindcasts from GCMs, as in Bretherton et al. (2019). This approach is applied to evaluate version
282 6 of the Community Atmosphere Model (CAM6), which uses the MAM4 aerosol scheme
283 detailed in Liu et al. (2016). CAM6 SOCRATES simulations and microphysics are described in
284 detail by Gettelman et al. (2020). CAM6 is nudged by wind, temperature, and surface pressure
285 fields from MERRA2 reanalysis (Gelaro et al., 2017) with a 1-day relaxation timescale. This
286 ensures the large-scale structure of simulated storms are close to the reanalysis, enabling
287 simulation of similar profiles of clouds, humidity, and aerosols in the model when compared to
288 aircraft observations at a given location and time. Clouds, humidity, and aerosols are not nudged
289 in CAM6, allowing a critical appraisal of their accuracy using the GV measurements. Model data
290 are co-located to observations by linearly interpolating to temporal and spatial locations from the
291 2 min x 50 m observational composites (Section 2.1) for CSET and SOCRATES.

292 We focus on comparing the observed aerosol and N_d concentrations with CAM6. CAM6
293 in-cloud N_d is computed as N_d divided by liquid cloud fraction (when cloud fraction $\leq 10\%$, we
294 set $N_d=0$). CAM6 aerosol number concentrations are computed using a bounded log-normal
295 distribution (Zender, 2001) for each of the instrument specified diameter ranges (D_{\min} to D_{\max}):

$$296 \quad N(D_{\min}, D_{\max}) = \frac{N_0}{2} \left[\operatorname{erf} \left(\frac{\ln(D_{\max}/D_m)}{\sqrt{2} \ln(\sigma_m)} \right) - \operatorname{erf} \left(\frac{\ln(D_{\min}/D_m)}{\sqrt{2} \ln(\sigma_m)} \right) \right] \quad (2)$$

297 where σ_m is the modal width parameter, D_m is the modal diameter, and N_0 is the modal number
298 concentration for each of the four modes in MAM4. The modal width parameter is 1.6 for
299 accumulation, Aitken, and primary carbon modes and 1.2 for the coarse mode. The modal
300 number contribution for both interstitial and out-of-cloud aerosol in the specified diameter range
301 is calculated using (2). The individual mode contributions are summed to produce the total,
302 instrumentally-matched CAM6 number concentration. These values can be directly compared
303 with observations because both count the number of particles within a specified size range.

304 Two instrumentally-matched values are calculated using the bounded log-normal: CN
305 (0.011 – 30 μm) and UHSAS100 (0.1 – 1 μm). Results using this model-derived UHSAS100 are
306 similar to CAM6 CCN concentrations at a supersaturation of 0.2% for SOCRATES (CCN at
307 0.2% (Sanchez & Roberts, 2018) is the closest proxy for UHSAS100 observationally, Figure
308 S2). However, CCN was not measured during CSET so no comparable relationship can be
309 deduced. The more complex but exact method of using a bounded log-normal distribution for
310 comparing modeled and observed aerosol number concentrations is thus necessary.

311 **3 Results**

312 **3.1 Synoptically Generated Recent Particle Formation**

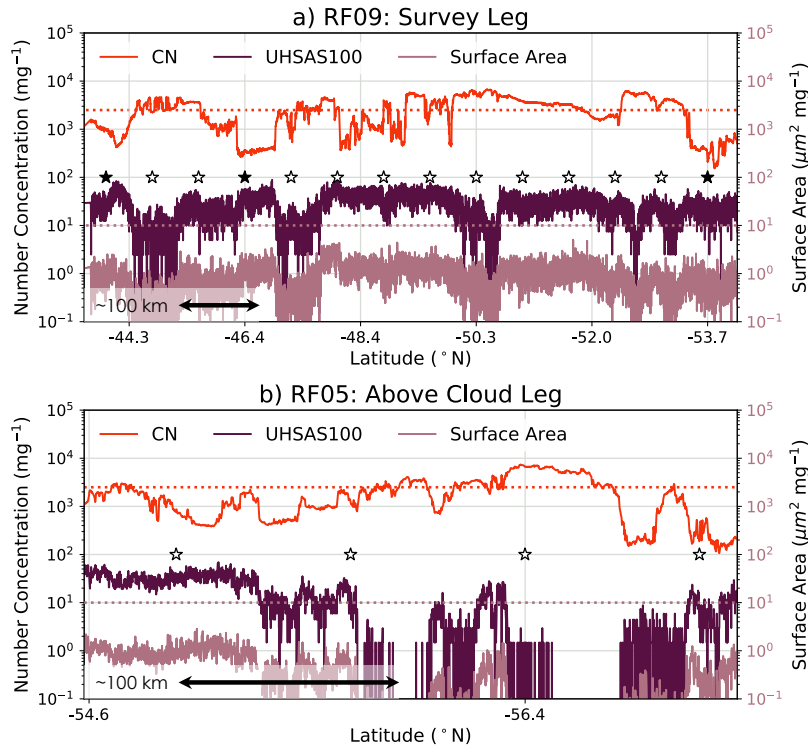
313 *3.1.1 Observations of Recent Particle Formation in the Southern Ocean and Sub-Tropics*

314 Evidence of recently formed particles occurring in the SO FT was observed frequently
315 during SOCRATES. Two example flight segments (Figure 2) have been selected to show the
316 simultaneously-occurring signatures that suggested recent particle formation: a MT survey leg

317 (Figure 2a, ~6 km altitude, 1200 km long) and an AC leg (Figure 2b, ~3 km altitude, 300 km
318 long). The first characteristic is large CN concentrations ($\geq 1000 \text{ mg}^{-1}$ and often exceeding 2500
319 mg^{-1}), which often varied rapidly (up to tenfold changes in concentration over a few km). CN
320 variability possibly marks recent bursts of particle formation or boundaries between different air
321 masses at different stages of nucleation (Clement et al., 2002). The second notable characteristic
322 is anti-correlation between UHSAS100 and CN concentrations (Covert et al., 1996) (i.e. low
323 UHSAS100 occurring with high CN). Finally, SA estimated from coarse and accumulation mode
324 particles is below the threshold enabling new particle formation ($\text{SA} \leq 10 \mu\text{m}^2 \text{mg}^{-1}$) (Clarke et
325 al., 1998; Covert et al., 1996).

326 Based on these signatures of recent particle formation, we use the maximum CN
327 concentration for a 10-minute flight segment ($\text{CN}_{\text{Max}10}$) to identify likely recent particle
328 formation (RPF) events in this pristine environment. We find that the upper quartile of $\text{CN}_{\text{Max}10}$
329 across the campaign ($\text{CN}_{\text{Max}10} \geq 2500 \text{ mg}^{-1}$) captures the majority of RPF cases observed. We
330 define the lower three quartiles ($\text{CN}_{\text{Max}10} < 2500 \text{ mg}^{-1}$) as unclear or non-RPF cases. This
331 restrictive methodology allows us to be confident in identifying RPF events for statistical
332 analysis of associated air mass histories and driving mechanisms (see Section 3.1.2). Instances of
333 $\text{CN} \geq 1000 \text{ mg}^{-1}$ are likely also associated with RPF but may be more aged (e.g. older,
334 coagulated Aitken particles) and have less distinct air mass histories. RPF identified by the
335 $\text{CN}_{\text{Max}10}$ criteria are indicated in Figure 2 and corresponding air mass trajectories can be seen in
336 Figure S3.

337 Clement et al. (2002) found that recently formed sulfuric acid particles in the upper
338 troposphere grew to observable sizes ($\sim 0.0125\text{-}0.03 \mu\text{m}$, comparable to our CN observation
339 limit of $0.011 \mu\text{m}$) within $\sim 5\text{-}10$ hours. While their analysis used different instrumentation and
340 occurred in the outflow of a mid-latitude storm system, this estimate is useful for interpreting
341 timescales of particle growth during SOCRATES. Based on this, recently formed particles
342 observed during SOCRATES are assumed to be within at least 5-10 hours of new particle
343 formation though may be more aged.



344
 345 *Figure 2 Example cases for suspected recent particle formation events observed in (a) survey-leg sampling in the mid-*
 346 *troposphere during RF09, and (b) above-cloud leg sampling during RF05. Observations are shown against time as flight*
 347 *proceeded south (note difference in length scale between a and b). Number concentrations (left axis) for total (CN, orange) and*
 348 *accumulation mode (UHSAS100, purple) particles. Surface area for coarse and accumulation mode aerosol (right axis, pink).*
 349 *Dotted lines for 2500 mg⁻¹ (orange) and 10 μm² mg⁻¹ (pink) are included for reference. HYSPLIT trajectory initial locations are*
 350 *marked, solid stars for non-RPF events (CN_{Max10}<2500 mg⁻¹) and open stars for RPF events (CN_{Max10}>2500 mg⁻¹).*
 351 *Corresponding HYSPLIT trajectory ascent profiles are shown in Figure S3.*

352 The SO FT is dominated by small aerosol particles (diameters < 0.1 μm) (Figure 3,
 353 orange). All SOCRATES flight data for CN and UHSAS100 is split by altitude, screened for
 354 cloud and drizzle, and used to compute normalized pdfs for three altitude segments (following
 355 regions defined in Figure 1): mid-troposphere (MT: $Z \geq 4.5$ km, a and b), above-cloud (AC: 1.5
 356 $\leq Z \leq 4.5$ km, c and d), and sub-cloud (SC: $Z \leq 1.5$ km, e and f). In both the MT and AC
 357 sampling, a significant percentage (~25%) of SOCRATES samples have $CN \geq 1000$ mg⁻¹ (Figure
 358 3b, d). These large FT CN concentrations are due to the prevalence of Aitken mode particles
 359 since the UHSAS100 pdfs at these levels rarely exceed 100 mg⁻¹ (<1%, Figure 3a, c).

360 Concentrations of $CN \geq 2500$ mg⁻¹ are less frequent in the sub-cloud layer (<1%
 361 compared to ~15% in the FT), suggesting MBL new particle formation is rare. However, Aitken
 362 aerosol particles are prominent in the MBL: the SC CN pdf retains significant probability near
 363 1000 mg⁻¹ (~15%) while SC UHSAS100 concentrations greater than 200 mg⁻¹ are rare (~5%)
 364 (Figure 3e, f). UHSAS100 pdfs exhibit a small shift to higher frequencies with decreasing
 365 altitude between MT and AC (from ~25 to ~35 mg⁻¹ in the median) and a larger shift between
 366 AC and SC (~35 to ~60 mg⁻¹ in the median) indicating some coagulation and growth is occurring
 367 as particles descend. The larger AC-SC change is consistent with cloud processing and
 368 condensational growth within the MBL being important for increasing accumulation mode
 369 concentrations.

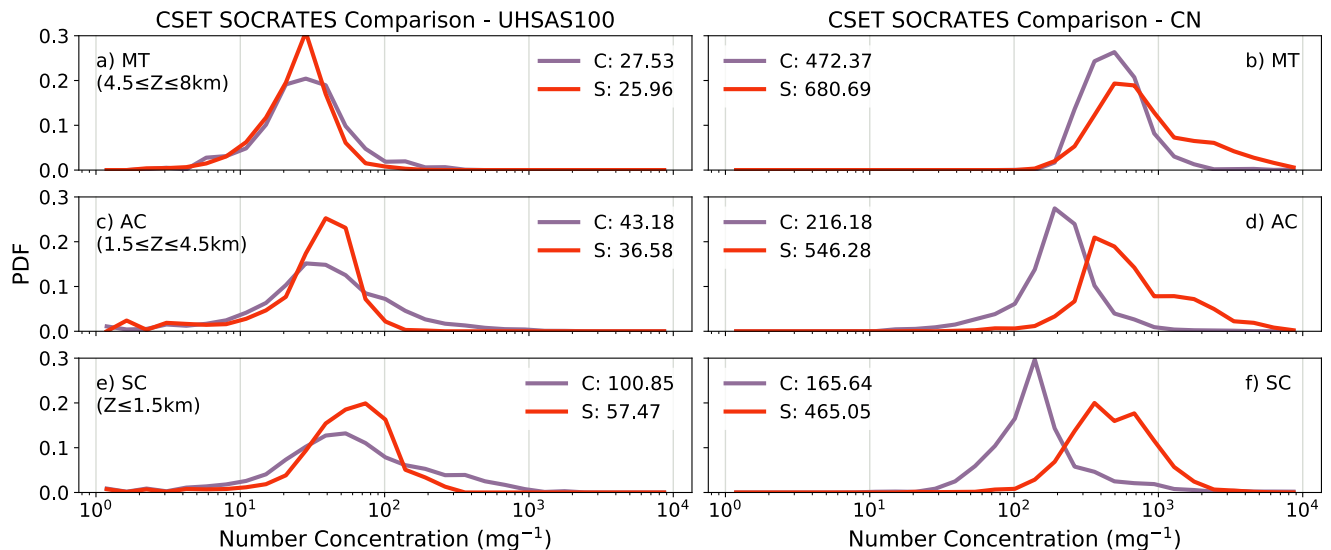
370
371
372373
374
375
376

Figure 3 Pdfs of number concentrations for UHSAS100 (a, c, e) and CN (b, d, f) for different altitudes: mid-troposphere (a, b), above cloud (c, d), and sub-cloud (e, f). Altitudes used for each range are listed in a, c, and e. SOCRATES observations (S, orange) are contrasted with CSET observations (C, purple). Median values are included for comparison.

377 To determine the uniqueness of the SO aerosol vertical structure and distribution, we
 378 contrast the height-matched SOCRATES number concentration pdfs with comparable pdfs in a
 379 typical sub-tropical environment sampled during CSET (Figure 3, purple). At all altitude levels,
 380 subtropical UHSAS100 occurs both for a wider range of concentrations and more frequently at
 381 high concentrations compared to SO observations (Figure 3a, c, e). Lower and less variable CN
 382 concentrations typify CSET compared to SOCRATES, indicating lower Aitken mode
 383 concentrations in the subtropics than over the SO. However, regional differences in Aitken mode
 384 concentrations vary vertically: SC CN pdfs are the most separated (Figure 3f) while MT CN pdfs
 385 are the most similar (Figure 3b) between campaigns.

386 These results have several implications for SO aerosol sources. If local, wind-driven sea-
 387 spray production was responsible for driving MBL aerosol number production in the SO, we
 388 would expect a higher ratio of UHSAS100 to CN concentrations in SOCRATES where winds are
 389 stronger compared to CSET (means of 14 vs. 7 m s⁻¹ within 200 m of the surface). This is
 390 opposite the observed behavior (Figure 3e, f), signaling that primary aerosol production is not the
 391 largest contributor to CN in the SO. While CN number concentration may not be driven by sea
 392 spray production, increased surface gas emissions associated with higher wind speeds (Lana et
 393 al., 2011) may still assist in secondary aerosol production and in growing aerosols in the SO.

394 Sub-tropical aerosols sampled in CSET were, in general, more aged than SO aerosols
 395 sampled in SOCRATES. CSET observations at 6 km typically had a low relative humidity (mean
 396 ~15 vs. ~30% during comparable SO sampling), implying a height of last saturation in the sub-
 397 tropics between 9-10 km. This is consistent with outflow from deep convective clouds, which
 398 can generate MT particles that subsequently coagulate as they slowly descend through the
 399 atmosphere (Clarke et al., 1998; Williamson et al., 2019). MT CN concentrations exceeding
 400 1000 mg⁻¹ occur less frequently during CSET than SOCRATES (~10% vs. ~30%) while MT
 401 UHSAS100 exceeding 100 mg⁻¹ occur occasionally (~2% vs. none), consistent with sampling

402 more aged aerosols in the sub-tropics which have descended from nucleation events above 6 km
 403 (Figure 3a, b). There are no instances of MT or AC $CN \geq 2500 \text{ mg}^{-1}$ during CSET (Figure 3b, d),
 404 indicating SO aerosol is more recently formed and sub-tropical RPF is rare at these altitudes.
 405 Continued aging with descent explains the rare occurrence of $CN \geq 1000 \text{ mg}^{-1}$ AC and SC in
 406 CSET compared to SOCRATES (none vs. $\sim 25\%$ AC, $<1\%$ vs. $\sim 15\%$ SC, Figure 3d, f).
 407 Coagulation and growth processes are also more active in the sub-tropics than the SO, consistent
 408 with Clarke et al. (1998): during CSET compared to SOCRATES, UHSAS100 pdfs shift with
 409 descent to larger concentrations (~ 25 to ~ 45 to ~ 100 vs. ~ 25 to ~ 35 to $\sim 55 \text{ mg}^{-1}$ in the median),
 410 CN to smaller (~ 470 to ~ 215 to ~ 165 vs. ~ 680 to ~ 550 to $\sim 465 \text{ mg}^{-1}$ in the median) (Figure 3c, d
 411 to e, f).

412 *3.1.2 Evidence for Particle Generation through Synoptic Uplift Mechanism*

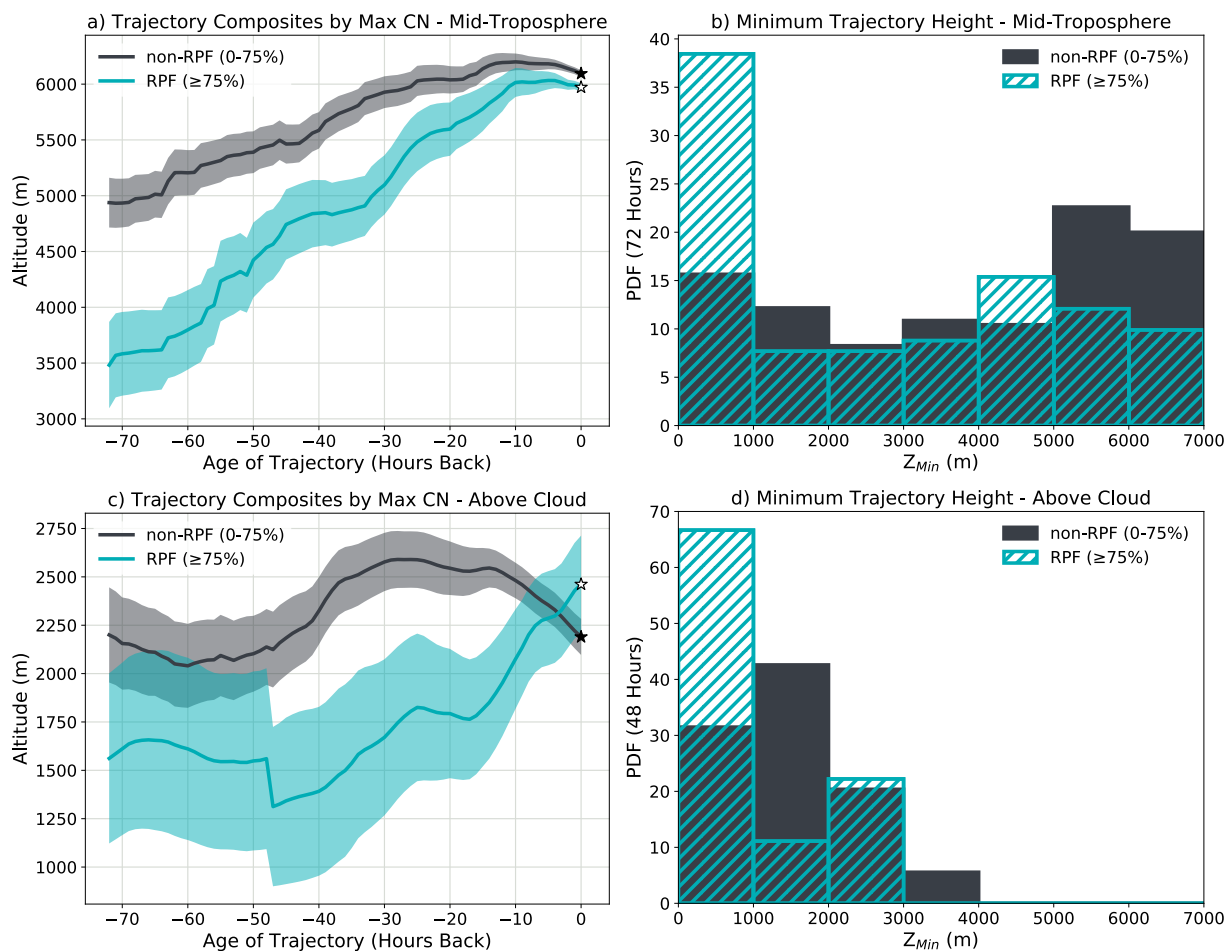
413 Remarkably high concentrations of Aitken mode aerosol particles frequently occur in the
 414 lower SO FT. Preceding studies (Section 1, e.g. Clarke et al. (1998), Weber et al. (2001)) have
 415 identified multiple forms of cloud outflow particle production mechanisms taking place over the
 416 SO. However, these mechanisms do not fully explain the quantity or location of RPF observed in
 417 the AC and MT layers during SOCRATES (Figure 3d, b). Clarke et al. (1998) identified new
 418 particle formation in outflow from cumulus congestus rising above the mean SO MBL.
 419 SOCRATES sampled infrequently in or downwind of such regimes. Weber et al. (2001)
 420 observed new particles and sulfuric acid vapors in the outflow of a frontal system off of
 421 Tasmania at ~ 6 km. SOCRATES observed RPF near a similar frontal system but not all MT
 422 events were associated with this type of feature. New particles have been observed in outflow
 423 regions of deep convection in the subtropics and mid-latitudes (Kerminen et al., 2018) which,
 424 along with frontal systems and general convective vertical motion, Covert et al. (1996)
 425 hypothesized were essential in generating FT Aitken particles. However, high concentrations of
 426 Aitken particles and RPF were observed on most SOCRATES flights and across a range of
 427 weather regimes with little evidence of recent penetrative congestus convection upstream.

428 SOCRATES provides the first opportunity to statistically analyze SO RPF events and
 429 holistically understand the particle production mechanisms generating them. Based on the
 430 frequent detection of RPF across varied weather regimes and altitudes during SOCRATES, and
 431 building on these earlier studies, we hypothesize that synoptic scale motions routinely generate
 432 new particles in the summertime SO FT. New particles are formed and dispersed after boundary-
 433 layer air is lifted and processed through precipitating clouds forming in regions of synoptic scale
 434 ascent. Two vital steps for gas to particle formation (Section 1) occur during synoptic-uplift: i)
 435 aerosol SA in the air mass is reduced during uplift through collision-coalescence processes
 436 associated with clouds and precipitation, and ii) DMS (and/or DMS-oxidation products) is lofted
 437 from the surface to an environment where it can oxidize, undergo photochemical reactions, and
 438 nucleate into new particles instead of depositing onto pre-existing aerosol particles (Covert et al.,
 439 1996; Kerminen et al., 2018; Seinfeld & Pandis, 2016; Weber et al., 2001).

440 We test this synoptic uplift mechanism by examining the altitude history of the MT air
 441 masses sampled in SOCRATES using RPF and non-RPF identified HYSPLIT 72-hour back
 442 trajectories (Figure 4a, b) (Section 2.2). RPF air masses exhibit a much steeper composite ascent
 443 profile over the past 72-hours compared to the non-RPF composite profile (Figure 4a). During
 444 the ascent period (10 to 70 hours back), the mean ascent rate for the RPF cases (1.1 cm s^{-1}) is
 445 comparable with estimates of the characteristic vertical velocity in mid-latitude synoptic systems
 446 ($\sim 1 \text{ cm s}^{-1}$) (Holton & Haikm, 2013). The non-RPF cases have significantly slower mean ascent

447 rates (0.6 cm s^{-1}). The deep uplift of the RPF air masses presumably creates thick precipitating
 448 clouds, which process and remove accumulation and coarse mode aerosols. RPF cases also
 449 originate from below 1 km more frequently in the preceding 72 hours compared to non-RPF
 450 cases (Figure 4b). Thus, RPF trajectories have the opportunity to source the necessary precursor
 451 gases (e.g. DMS) from the boundary-layer, which is necessary for gas to particle conversion to
 452 take place.

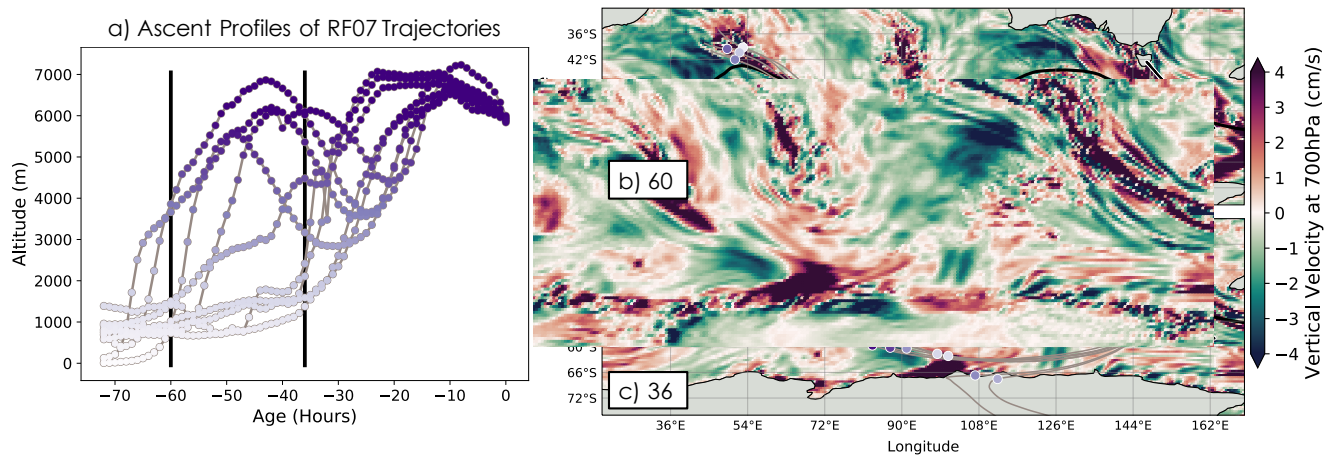
453 AC RPF events are similarly examined (Figure 4c, d). There is a clear distinction
 454 between the RPF and non-RPF cases in the 48 hours prior to sampling: the RPF case composite
 455 shown in Figure 4c has a rapid synoptic ascent profile (1 cm s^{-1} in the last 20 hours) and most
 456 RPF back-trajectories come from below 1 km (Figure 4d). On average, the non-RPF trajectories
 457 show zero mean ascent over the previous 72 hours.



458
 459 *Figure 4 Mean (line) and its corresponding standard error (shading) of ascent profiles for HYSPLIT trajectories initiated in the*
 460 *mid-troposphere (a) and above cloud (c). Corresponding distributions of minimum height over preceding time where altitude*
 461 *profiles are statistically distinct: 72-hours for mid-troposphere (b) and 48-hours for above cloud (d). Trajectories are composited*
 462 *by CN_{Max10} into RPF events (blue, $CN_{Max10} \geq 75^{th}$ percentile) and non-RPF events (gray, $CN_{Max10} < 75^{th}$ percentile). Number of*
 463 *RPF vs non-RPF cases per SOCRATES research flight for mid-troposphere and above-cloud are shown in Figure S4.*

464 We use ECMWF ERA5 reanalysis to investigate the large-scale synoptic patterns driving
 465 the uplift associated with SO RPF. Flight RF07 is used as an example to demonstrate the typical
 466 synoptic patterns responsible for RPF events, as many RPF identified back-trajectories occurred
 467 during its survey leg ($\sim 6 \text{ km}$) (Figure 5). Rapid ascent from the MBL on these back-trajectories

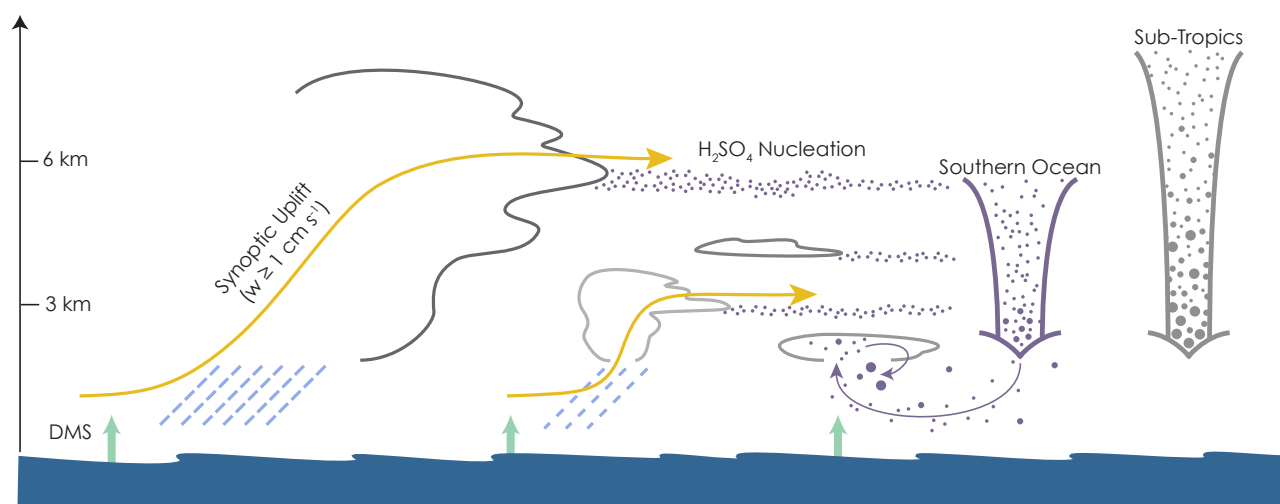
468 occurred in two periods: ~60 hours (Figure 5a, b) and ~36 hours (Figure 5a, c) prior to GV
 469 sampling. Vertical velocity and geopotential height fields at 700 hPa (chosen as a representative
 470 mid-level altitude) help to identify the cause of this uplift: a warm conveyor belt (WCB). The
 471 WCB moves along an eastward propagating Rossby wave (traced by a representative
 472 geopotential height contour in Figure 5b, c). At ~60 hours (Figure 5b), a tongue of warm, moist
 473 MBL air from the sub-tropics is advected up towards the mid-troposphere and poleward ahead of
 474 the cold front (42°S, 54°E). At ~36 hours (Figure 5c), trajectories off the edge of Antarctica
 475 (60°S, 100°E) undergo uplift associated with the remains of the WCB that has traveled along the
 476 Rossby wave. The WCB generates potential vorticity anomalies that drive the upward motion
 477 responsible for RPF. Sub-polar vortices (e.g. 60°S, 70°E and 54°S, 140°E, Figure 5c) led to
 478 uplift of MBL air to the MT in other research flight cases but did not affect the trajectories
 479 sampled during RF07.



480
 481 *Figure 5 Illustration of synoptic scale patterns influencing MT RPF identified air masses sampled by RF07 (black line from*
 482 *Tasmania, b and c). Two times of uplift are of note (ascent marked by black lines in a): 60 (b) and 36 (c) hours prior to GV*
 483 *sampling. ERA5 reanalysis maps at these times of interest include 700 hPa vertical velocity (colors) with a reference 700 hPa*
 484 *geopotential height contour at 2.9 km (black contour). The geopotential height contour separates warmer, moister sub-tropical*
 485 *air from cooler, drier polar air and marks the Rossby wave propagating to the East. RPF trajectories (gray lines) with air mass*
 486 *locations (circles) colored by their altitude (white to purple, as in the ascent profiles in a). Ascent of the first set of trajectories at*
 487 *60-hr (b) occurs off the tip of Africa while ascent of the 36-hr trajectories (c) occurs off the coast of Antarctica, both driven by*
 488 *the advance of a warm-conveyor belt towards the south east (i.e. along the height contour and Rossby wave). Note sub-polar*
 489 *vortices affecting the vertical velocity in c) at 60°S, 72°E and 54°S, 140° E. An animation of the RF07 synoptic event is included*
 490 *in supplemental material, MS01.*

491 Synoptic analysis of all SOCRATES flights reveals that uplift along RPF trajectories is
 492 typically associated with either warm conveyor belts or sub-polar vortices. The particle
 493 production observed in cloud outflow from a frontal system by Weber et al. (2001) would be
 494 considered a WCB example of the synoptic-uplift mechanism. In the southern hemisphere,
 495 WCBs are not always associated with cyclones and occur frequently off the tip of South America
 496 and South Africa (Catto et al., 2015). WCBs are also not as constrained in longitude in the
 497 southern hemisphere as in the northern hemisphere, occurring frequently across a wide range of
 498 longitudes in the SO (Eckhardt et al., 2004). The behavior of MT RPF back trajectories is
 499 consistent with both these characteristics of WCB behavior in the SO: i) the typical RPF
 500 trajectory path arcs down from South Africa towards Antarctica, funneling along the large-scale
 501 waves in the region, and ii) the geographic location of minimum RPF trajectory altitudes is
 502 widespread across the SO (Figure S5).

503 Widespread and frequent RPF occurrence across the summertime SO free troposphere is
 504 ensured due to the regularity of synoptic uplift (i.e. aerosol cleansing and lofting of air masses to
 505 favorable environments for gas to particle formation) and ubiquitous, DMS-rich boundary-layer
 506 air (i.e. air masses enriched in precursor gases, ensured by many regions with significant DMS
 507 fluxes in the austral summer (Lana et al., 2011)). The synoptic-uplift mechanism (Figure 6)
 508 works together with other particle formation mechanisms in the region (Clarke et al., 1998) to
 509 create a free troposphere that is frequently rich in Aitken particles. This has a profound impact
 510 on N_d and ACI in the SO, as will be discussed in Section 3.2.



511
 512 *Figure 6 Diagram of aerosol generation and cycling associated with the novel synoptic uplift mechanism for new particle*
 513 *formation. Yellow arrows signify synoptic motions (vertical velocity $\geq 1 \text{ cm s}^{-1}$) responsible for particle generation. Differences*
 514 *in the vertical distribution of aerosols as they descend are highlighted for the Southern Ocean (purple) and sub-tropics (gray)*
 515 *based on tendencies highlighted in Figure 3 (comparison modeled after Clarke et al. (1998)).*

516 3.1.3 Southern Ocean Summertime Aerosol Composition Estimations

517 If new particle formation generated through synoptic uplift (Figure 6) is a major source of
 518 FT Aitken aerosols, we expect to find signatures of DMS oxidation products in FT particles
 519 sampled during SOCRATES. Ambient aerosol measurements from behind the CVI (Section 2.1)
 520 support this speculation and provide additional insights into the size and composition of SO
 521 aerosol in the summertime: i) Aitken and the few, small accumulation mode ($\leq 0.2 \mu\text{m}$) particles
 522 occurring in high number concentration samples in the FT are composed primarily of H_2SO_4
 523 with possible contributions from more volatile DMS oxidation products like MSA; ii) the
 524 majority of these Aitken particles in the FT are smaller than $0.02 \mu\text{m}$ in diameter; and iii)
 525 accumulation-mode particles ($\sim 0.1\text{-}0.5 \mu\text{m}$) sampled from AC, IC, and SC flight levels are
 526 primarily sulfur-based with limited sea spray influence (Twohy et al., 2021).

527 FT Aitken particle composition is assessed using a particle volatility estimate (Section
 528 2.1) based on the temperature evolution of the ratio between heated and unheated CN, $\text{CN}_{\text{CVI}}/\text{CN}$
 529 (Figure 7). Limited sampling occurred where both high aerosol concentrations were present and
 530 CVI temperatures were cycled, requiring our analysis to be expanded beyond RPF cases to all
 531 instances where $\text{CN} \geq 800 \text{ mg}^{-1}$. Our examination is limited to the FT ($Z \geq 1.5 \text{ km}$) because it is
 532 dominated by the Aitken particles of interest (see level-leg median cumulative distributions for
 533 AC and MT, Figure S6) and the majority of the CVI temperature cycling experiments occurred
 534 in this altitude range.

535 FT Aitken-dominated samples predominantly contain highly volatile particles.
536 CN_{CVI}/CN decreases with increasing CVI temperature (Figure 7) when the ambient particles (-20
537 to -15°C , 450-500 hPa in the MT; -5 to 0°C , 750-850 hPa AC) are exposed to CVI maximum
538 temperatures (supplemental text S1) between ~ 25 - 60°C . The most dramatic particle number
539 decrease occurs for CVI maximum temperatures above ~ 25 - 30°C . Aitken volatilization to sizes
540 below the CN detection limit ($0.011\ \mu\text{m}$) under this imposed CVI temperature range is consistent
541 with previous volatility results for small H_2SO_4 particles (Clarke et al., 1987). H_2SO_4 volatility is
542 a function of particle size with small particles volatilizing at much lower temperatures than larger
543 particles under the same conditions (Orsini et al., 1999). Greater than 30% decreases in diameter
544 have been observed for $0.015\ \mu\text{m}$ diameter particles at 25°C (Orsini et al., 1999) while $0.3\ \mu\text{m}$
545 particles begin losing mass at $\sim 30^{\circ}\text{C}$ and completely volatilize by 125°C (Clarke, 1991).
546 Conversely, neutralized nss- SO_4 (e.g. ammonium sulfate begins volatilizing above 200°C
547 (Clarke et al., 1987)) and sea spray aerosol (e.g. sodium chloride begins volatilizing at $\sim 600^{\circ}\text{C}$
548 (Jennings & O'Dowd, 1990; Jennings et al., 1994)) volatilize at even higher temperatures
549 (Schmid et al., 2002) and do not appear to contribute to the composition of the Aitken particles
550 observed in the FT during SOCRATES (Figure 7).

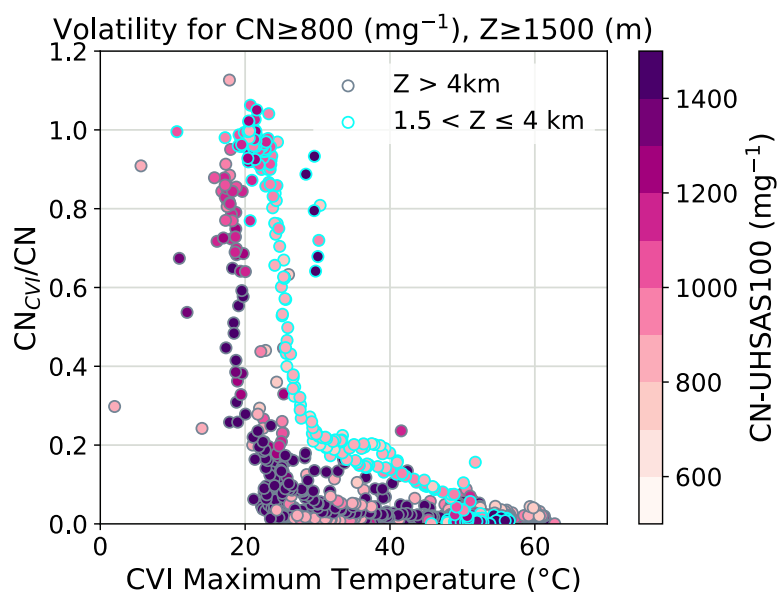
551 Not all sizes of pure H_2SO_4 particles will shrink below the CN detection limit within the
552 limited CVI temperature range (~ 25 - 60°C) maintained in SOCRATES. H_2SO_4 particles with
553 diameters $\geq 0.035\ \mu\text{m}$ required exposures to temperatures over 90°C for ~ 0.2 seconds before
554 shrinking to smaller than $0.011\ \mu\text{m}$ (Orsini et al., 1999). The longer residence time during
555 SOCRATES (~ 2 seconds) likely reduces the temperature required for volatilizing H_2SO_4 particles
556 below $0.011\ \mu\text{m}$. Unless particles are $< 0.02\ \mu\text{m}$, however, it would be difficult to shrink pure
557 sulfuric acid particles below the CN size threshold ($0.011\ \mu\text{m}$) at these temperatures ($\sim 30^{\circ}\text{C}$)
558 (Orsini et al., 1999). Assuming the observed Aitken particles are H_2SO_4 , their volatility at ~ 25 -
559 30°C (Figure 7) suggests the majority of particles are $\leq 0.02\ \mu\text{m}$. H_2SO_4 particles of comparable
560 sizes have exhibited similar behaviors (i.e. partially evaporating below 30°C) to our observations
561 (Orsini et al., 1999; Schmid et al., 2002).

562 Volatility signatures were also noted in the size-resolved accumulation mode UHSAS
563 measurements during the campaign, providing additional insight into FT particle composition.
564 Very few accumulation mode particles contribute to the Aitken-dominated FT samples analyzed
565 in this section ($\leq 50\ \text{mg}^{-1}$, Figure S7b) and most have diameters $\leq 0.2\ \mu\text{m}$ (Figure S6). However,
566 sufficient UHSAS100 samples occurred during CVI temperature cycles to produce a matched
567 volatility analysis for accumulation mode volatility aerosols (Figure S7).
568 $UHSAS100_{CVI}/UHSAS100$ decreases near ~ 25 - 30°C , similar to the CN ratio although likely
569 noisier due to the small number of accumulation mode particles sampled. The similarity of the
570 temperature inflection point for these two volatility ratio curves suggests that small accumulation
571 mode aerosols may share their origin with Aitken aerosols in these high aerosol concentration
572 events and that volatile DMS oxidation products are likely the leading contributor to the
573 composition of the few accumulation mode aerosols occurring in the FT (Figure 3a, c).

574 The magnitude of the particle size change in the small accumulation mode range
575 (shrinking from 0.1 - $0.2\ \mu\text{m}$ to below $0.1\ \mu\text{m}$) potentially signals the presence of aerosol species
576 with even higher volatility than H_2SO_4 (Orsini et al., 1999). The most likely candidate for an
577 additional volatile species contributing to particle composition over the SO is the DMS oxidation
578 product MSA, which has a higher vapor pressure than H_2SO_4 (Berresheim et al., 2002; Mauldin
579 et al., 1999). Relatively large MSA particles (0.16 - $0.26\ \mu\text{m}$) volatilize at ~ 50 - 60°C (O'Dowd et
580 al., 1997). The equilibrium vapor pressure of MSA depends on the availability of bases and RH

581 so this temperature range may not be applicable across all conditions (Hodshire et al., 2019).
 582 However, it is suggestive that small, recently formed MSA particles can evaporate at 30-35°C
 583 during the increased SOCRATES CVI residence time. MSA may also contribute to the
 584 separation between the AC and MT volatility curves (Figure 7, S4). Higher Aitken mode
 585 concentrations (\sim CN-UHSAS100, colors in Figure 7, S7a) were found in the MT relative to AC
 586 for the few samples available, possibly marking less coagulation and growth occurring after
 587 particle formation in the MT which would result in smaller, more volatile particles. These MT
 588 particles resided at lower ambient temperatures and slightly lower RH (Figure S6a) which, if
 589 MSA was present, could drive MSA to partition preferentially to the particulate phase
 590 (Berresheim et al., 2002), dominating the volatility response. While low temperatures favor MSA
 591 particulate phase partitioning, low RH does not (Hodshire et al., 2019). Understanding the
 592 observed accumulation and Aitken volatility responses and the nuances of their implications
 593 about particle composition requires more detailed measurements in future campaigns (e.g. gas
 594 composition and Aitken size resolved aerosol concentrations, Section 4).

595 STEM analysis of micro-impactor substrates taken during ambient CVI sampling during
 596 SOCRATES (Twohy et al., 2021) gives us further insight into MBL accumulation mode particle
 597 composition. For the cases analyzed, mean percentages show sulfur-based particles dominate the
 598 SO summertime accumulation mode (\sim 0.1-0.5 μ m) number concentration at all altitudes: 93%
 599 AC, 68% IC, and 70% SC. The small remaining number fraction is composed of salt-based sea
 600 spray, sometimes enriched with sulfur or other trace compositions. If small amounts of organic
 601 material occur in these samples, they are not detectable on the carbon STEM substrate. The
 602 dominant, sulfur-based composition of these accumulation-mode particles is consistent with
 603 most particles growing from Aitken mode aerosols composed of H₂SO₄ or other DMS oxidation
 604 products (Section 1). Implications of Aitken particle growth into accumulation mode sizes will
 605 be discussed further in Section 3.2.2.

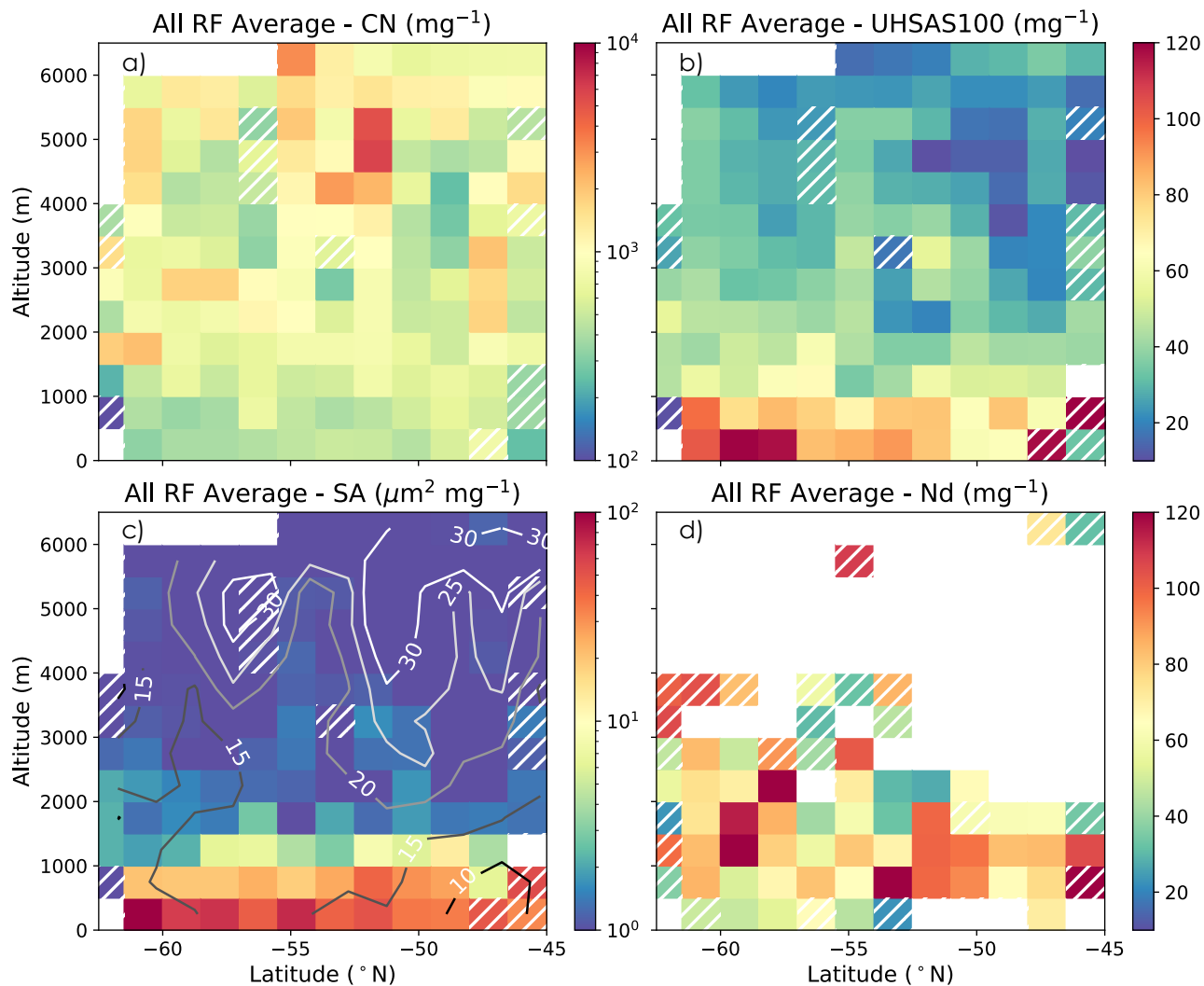


606
 607 *Figure 7 Volatility curves from CVI analysis presented as the ratio between CN and CN_{CVI} versus the maximum temperature of*
 608 *the CVI instrument (supplemental text S1). Points are shown for CN \geq 800 mg⁻¹ above which the small particle concentration is*
 609 *large enough to mark RPF or slightly grown nucleation mode aerosol. Points are limited to FT samples (Z \geq 1.5 km) due both to*
 610 *limited temperature cycling in the MBL and to targeting Aitken mode dominated environments (Figure S6). Outline colors denote*
 611 *altitude of sample: mid-troposphere (gray) and above cloud (blue). Points are colored by CN-UHSAS100 to estimate the number*
 612 *of particles in the Aitken mode (generally more in the mid-troposphere).*

613 **3.2 Controls on Southern Ocean Aerosol and Cloud Droplet Number**
 614 **Concentrations**

615 *3.2.1 Average Southern Ocean Aerosol and N_d Structures*

616 To better understand the factors influencing the generation and depletion of aerosols and
 617 cloud droplets in the SO and how synoptically generated Aitken particles influence the SO
 618 aerosol budget, it is useful to examine the spatial distribution of aerosol and cloud features as
 619 sampled by SOCRATES. Flight data is binned by altitude and latitude (Section 2.1) and a multi-
 620 flight, campaign average composite is generated for concentrations of aerosol number, aerosol
 621 surface area (SA, for coarse and accumulation mode as calculated in Section 2.1), and N_d (Figure
 622 8).



623 *Figure 8 All flight average composites of binned flight medians for 500 m x 1.5° boxes. Aerosol variables are screened for cloud*
 624 *and rain contamination. Number concentrations for (a) total aerosol, (b) accumulation mode aerosol, and (d) cloud droplets are*
 625 *shown along with (c) the surface area concentration computed from accumulation and coarse mode size distributions. Contours*
 626 *of all flight average composite wind speed are also included (c). Bins sampled by 2 or less flights are hatched to indicate*
 627 *inadequate sampling. A companion plot to (d) of cloud droplet number concentration in cm^{-3} units is in Figure S8.*
 628

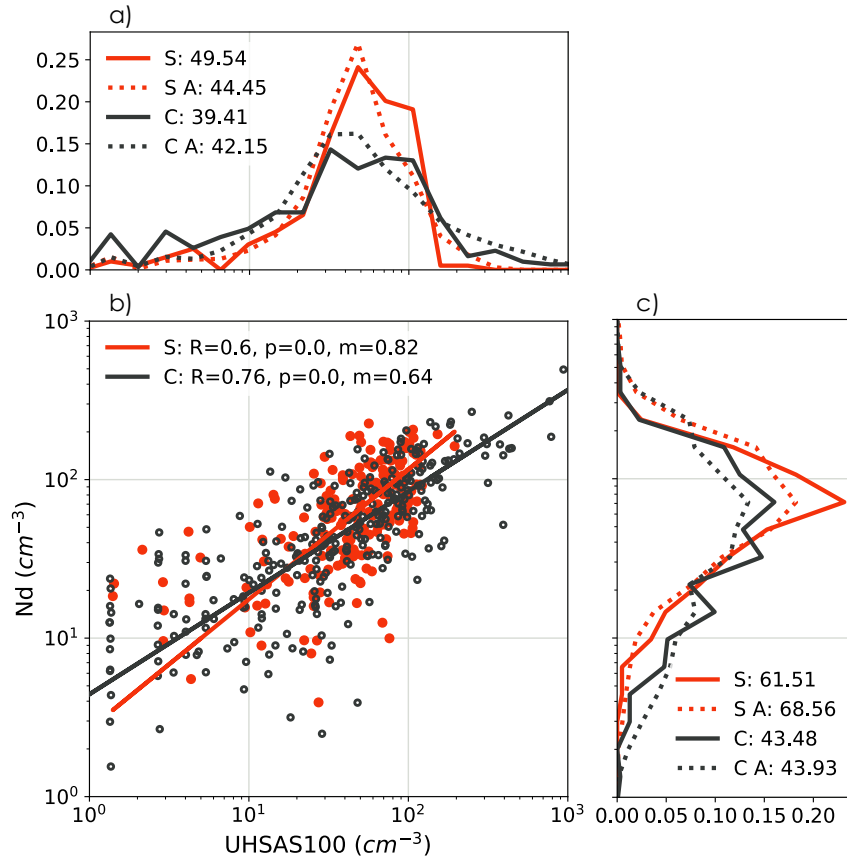
629 The mean SO CN does not vary significantly with latitude and maintains particle
630 concentrations on the order of $\sim 1000 \text{ mg}^{-1}$ in the FT ($\geq 1.5 \text{ km}$) and $\sim 500 \text{ mg}^{-1}$ in the MBL (< 1.5
631 km) (Figure 8a). This is consistent with the altitude trend in the CN histograms shown in Figure
632 3 (d, e, f). The prevalence of consistent high concentrations of CN in the FT across all latitudes
633 suggests synoptic generation (Section 3.1) exerts a widespread influence on SO Aitken mode
634 concentrations.

635 Accumulation mode number (Figure 8b) and SA (Figure 8c) concentrations both decrease
636 significantly with increasing altitude. SA is largest in the near-surface bins due to increased
637 production of large accumulation and coarse mode aerosols associated with sea spray (see wind
638 speed contours, Figure 8c). Coarse mode particles contribute 2 to 10 times more to total SA in
639 the MBL than accumulation mode (estimated from UHSAS100) while accumulation mode
640 dominates SA in the FT (Figure S9). UHSAS100 concentrations are largest sub-cloud but are
641 less clearly connected to the surface.

642 SA above $\sim 1.5 \text{ km}$ is consistently low enough ($\text{SA} \leq 10 \mu\text{m}^2 \text{ mg}^{-1}$) to support gas to
643 particle conversion (Clarke et al., 1998; Covert et al., 1996). While low SA is common in the FT,
644 it is rarely observed in the underlying MBL. The single exception occurred during RF13 which
645 sampled an extensive stratocumulus layer under an anticyclonic ridge. In this instance, low SA
646 and high, variable SC CN concentrations were observed in a narrow rift of precipitating shallow
647 cumuli but not in the surrounding stratocumulus-capped MBL. The lack of SC particle formation
648 signatures during SOCRATES is also shown in Figure 3f.

649 No clear latitudinal dependence in N_d was observed during SOCRATES (Figure 8c)
650 although a slight gradient in CCN was observed (Sanchez et al., 2021). A modest dip at $\sim 55^\circ\text{S}$
651 in N_d associated with increased precipitation in the mid-latitude storm track is expected in this
652 portion of the SO based on satellite climatology (I. L. McCoy et al., 2020) and is seen in
653 concurrent ship observations of aerosol between $55\text{--}60^\circ\text{S}$ (Sanchez et al., 2021). However, the
654 limited amount and spatial distribution of in-cloud sampling during SOCRATES is likely
655 insufficient to capture this nuance of N_d behavior. Cloud observations occur in more altitude bins
656 to the south, either a manifestation of the more frequent occurrence of multi-layered clouds in the
657 southern SO or the more frequent sampling in that region during SOCRATES. Most N_d samples
658 range between 60 and 100 or more mg^{-1} (similar in cm^{-3} , Figure S8) which is consistent with
659 satellite derived N_d climatologically (Bodas-Salcedo et al., 2019; Grosvenor et al., 2018; I. L.
660 McCoy et al., 2020) and instantaneously (Kang et al., 2021) sampled in this region and season.

661 Qualitatively, we see that the campaign average N_d is comparable to the SC UHSAS100
662 accumulation-mode aerosol concentration (Figure 8b, d). Quantitatively, N_d and UHSAS100 are
663 correlated at 95% confidence ($R=0.6$, Figure 9b) when comparing matched time by altitude bins
664 along individual flight composites. Similar distributions occur for matched and total binned
665 flight data for both N_d and UHSAS100, indicating behavior captured in the N_d -UHSAS100 space
666 is representative of SO cloud and aerosol tendencies (Figure 9a, c). Near-cloud UHSAS100
667 explains 36% of the variance in SO N_d . Consistently higher N_d values for corresponding
668 UHSAS100 (Figure 9a, c) indicates aerosol particles with diameters $\leq 0.1 \mu\text{m}$ are also activating
669 and contributing to N_d , but poor size-resolved sampling of these particles prevents quantification
670 (see Section 3.2.3 for further discussion). Level-leg median N_d measurements have a stronger
671 relationship with median sub-cloud level leg UHSAS100 ($R=0.52$) than with above-cloud
672 UHSAS100 ($R=0.28$) at 95% confidence (Figure S10), indicating SC accumulation mode aerosol
673 significantly influences SO N_d . We next examine the source of this aerosol in the SO.



674
 675 *Figure 9 Relationship between accumulation mode and cloud droplet number concentrations in SOCRATES (S, orange) and*
 676 *CSET (C, gray). (b) Altitude (50 m) vs time (2 minutes) bin medians for N_d and UHSAS100 are computed for each flight, matched*
 677 *by space and time, and compared. Pdfs of binned data when both N_d and UHSAS100 are present are shown as solid lines for (a)*
 678 *UHSAS100 and (c) N_d . Pdfs of total, unmatched binned flight data are shown as dashed lines (a, c) and marked with an A. Total*
 679 *data pdfs agree with the behavior of the matched subset. Corresponding median values (a, c), correlation coefficients and p-*
 680 *values (b), and slopes for a log-log fit (b) are included for reference. Few instances of precipitation-depleted N_d or N_d -*
 681 *UHSAS100 points occur ($\leq 10 \text{ cm}^{-3}$) in SOCRATES. CSET has a greater number of precipitation-depleted cloud and aerosol*
 682 *features (b, c).*

683 3.2.2 Sources of Accumulation Mode Aerosol in the Southern Ocean

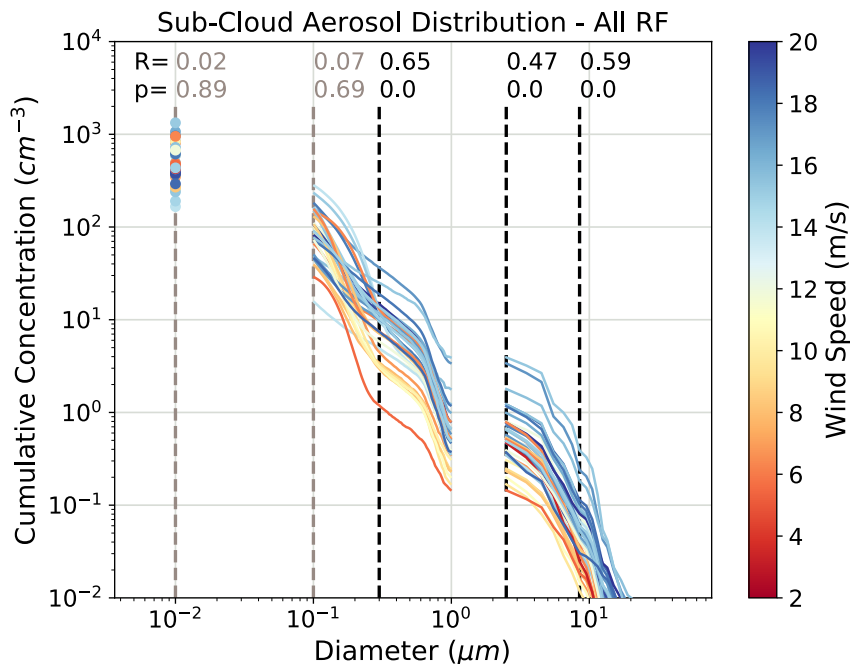
684 SC accumulation mode aerosol is the principal control on SO N_d (Section 3.2.1). In this
 685 pristine region, accumulation mode aerosol particles originate from i) primary sea spray
 686 emissions from the surface or ii) growth of Aitken mode aerosols generated through secondary
 687 aerosol processes, which can either occur locally in the MBL or in the FT and descend into the
 688 SC. Prior work suggests the latter behavior dominates SO summertime CCN (Covert et al., 1996;
 689 Korhonen et al., 2008; D. T. McCoy et al., 2015; Quinn et al., 2017; Raes, 1995) and that sea-
 690 spray aerosol has only a weak influence on CCN (Modini et al., 2015; Prather et al., 2013; Quinn
 691 et al., 2015). SOCRATES provides the opportunity to further test this. Median SC level leg
 692 (sampled for ≥ 5 minutes) cumulative distributions (Section 2.1) are calculated and colored by
 693 the corresponding median wind speed (Figure 10). Wind speed is a common proxy for estimating
 694 sea spray production (Grythe et al., 2014) as well as the magnitude of surface gas fluxes.
 695 Correlations are calculated between wind speed and the log of the cumulative number
 696 concentration (Grythe et al., 2014) at progressive diameter intervals to understand the influence
 697 of wind-speed mechanisms at different aerosol sizes.

698 Wind-speed dependent production mechanisms are not the main control on small
 699 accumulation and Aitken mode concentrations, as exhibited by the lack of correlation when these
 700 small particle sizes are included (R for diameters ≥ 0.011 , $\geq 0.1 \mu\text{m}$ in Figure 10). Conversely,
 701 coarse (R for ≥ 2.5 , $\geq 8.5 \mu\text{m}$) and larger accumulation mode (R for $\geq 0.3 \mu\text{m}$) aerosol number
 702 concentrations are positively and significantly correlated at 95% confidence with wind speed.
 703 Thus, larger particles (diameters between $0.3\text{-}30 \mu\text{m}$) are likely connected to sea spray
 704 production mechanisms, consistent with earlier studies (Grythe et al., 2014) (also see Figure 8c).

705 Enhanced growth associated with increased DMS fluxes (Lana et al., 2011) or increased
 706 contributions of submicron organics to sea spray (O'Dowd et al., 2008) may additionally
 707 contribute to wind-speed correlations for accumulation and coarse mode aerosols. However, little
 708 submicron organic mass was observed in the MBL during concurrent ship sampling and when
 709 present it was dominated by sulfate mass (a ratio of 0.2 when submicron organic mass was above
 710 its detection limit) (Twohy et al., 2021). This suggests organics have a relatively minor
 711 contribution to summertime CCN as measured by SOCRATES, as previously observed for
 712 similar SO latitudes (Fossum et al., 2018), although recent work suggests organics have some
 713 influence on particles smaller than $0.15 \mu\text{m}$ (Saliba et al., 2020).

714 Size ranges that contribute the majority of particles ($0.01\text{-}0.3 \mu\text{m}$), and the majority of the
 715 CCN ($0.1\text{-}0.3 \mu\text{m}$), have no relationship with wind speed (Figure 10), consistent with mainly
 716 sulfur-based ($0.1\text{-}0.5 \mu\text{m}$ diameters) and sulfuric acid ($\leq 0.02 \mu\text{m}$ diameters) composition
 717 signatures (Section 3.1.3). FT Aitken aerosols clearly play an essential role in developing SO
 718 accumulation mode aerosol and in SO ACI. The nuances of Aitken influence on N_d are discussed
 719 in the next section.

720
 721



722
 723 *Figure 10 Cumulative size distributions for median sub-cloud level-leg aerosol (calculated for legs with at least 5 minutes of*
 724 *sampling) colored by wind speed at the aircraft (~150 m). Aerosol number concentrations from CN (dots, $\geq 0.01 \mu\text{m}$), UHSAS*
 725 *(accumulation, $0.1\text{-}1 \mu\text{m}$, middle curves), and CDP (coarse, $2.5\text{-}30 \mu\text{m}$, right curves) are screened for cloud and drizzle. The*

726 cumulative distribution is summed from right to left where CN equals the total number concentration. Correlation coefficients
 727 and p-values computed between wind speed and the log of the cumulative number concentrations to the right of the dashed lines
 728 are marked (gray for not significant and black for significant at 95% confidence). The relationship between wind speed and
 729 \log_{10} (cumulative aerosol number concentration) weakens with a decrease in diameter.

730 3.2.3 Influence of Aitken Mode Aerosols on Southern Ocean Summertime Cloud Droplet 731 Number Concentrations

732 SOCRATES observations have verified that the FT is a large reservoir of Aitken mode
 733 aerosols. Once subsided or entrained into the MBL, these particles may contribute to CCN
 734 (Section 3.2.2) and help to modulate SO N_d . Low level clouds in the SO produce a large
 735 precipitation sink in N_d and CCN (I. L. McCoy et al., 2020). Despite the magnitude of this sink,
 736 relatively high mean SO droplet number concentrations are maintained ($N_d \sim 80\text{-}100 \text{ cm}^{-3}$) (I. L.
 737 McCoy et al., 2020). For this to be possible, a large and persistent source of CCN must exist over
 738 the SO.

739 The small ($\leq 0.02 \mu\text{m}$, Section 3.1.3) FT Aitken mode particles brought into the MBL are
 740 unlikely to be activated as CCN, even in the stronger updrafts typically occurring in SO marine
 741 low clouds. Thus, they likely grow to larger Aitken sizes first, through a combination of
 742 condensational growth from the deposition of DMS oxidation products (Ayers et al., 1997; Ayers
 743 & Gillett, 2000; Ayers & Gras, 1991; Bates et al., 1998; Charlson et al., 1987) and organic gases
 744 (Saliba et al., 2020; Zheng et al., 2020).

745 A buffering mechanism can occur in response to precipitation sinks. Coalescence
 746 scavenging of N_d reduces aerosol number concentration (Wood et al., 2012) and aerosol surface
 747 area, leading to increased peak supersaturation during subsequent activation events for a given
 748 updraft speed. This results in activation of smaller aerosols, including some of the larger Aitken
 749 mode particles which can subsequently grow to accumulation mode sizes through uptake of SO_2
 750 in cloud (Kaufman & Tanré, 1994). Thus, instead of precipitation leading to N_d reduction and
 751 eventual cloud breakup (as seen in a low-aerosol, high N_d cloud chamber test by Chandrakar et
 752 al. (2017)), the reservoir of FT Aitken aerosol may buffer N_d against precipitation depletion.

753 Supportive of this hypothesis, we observe fewer precipitation-depleted cloud and aerosol
 754 features (N_d , UHSAS100 $\leq 10 \text{ cm}^{-3}$) during SOCRATES relative to CSET (Figure 9). Both
 755 campaigns sampled intermittently precipitating shallow cumulus and stratocumulus clouds: SO
 756 cyclone cold sectors in SOCRATES and the NEP stratocumulus to trade cumulus transition in
 757 CSET. The SO and NEP both experience frequent low cloud precipitation (Leon et al., 2008).
 758 Similar near-cloud median accumulation mode aerosol concentrations occurred during
 759 SOCRATES ($\sim 50 \text{ cm}^{-3}$) and CSET ($\sim 40 \text{ cm}^{-3}$) when sampling far from continents (Figure 9a).
 760 Despite this, median N_d is higher and less variable during SOCRATES compared to CSET (~ 70
 761 vs. $\sim 40 \text{ cm}^{-3}$, Figure 9c).

762 The frequent occurrence of precipitation-depleted clouds ($N_d \leq 10 \text{ cm}^{-3}$) in the cumulus
 763 regime west of 140°W defines the lower tail of the N_d CSET pdf (Figure 9c). These ‘veil cloud’
 764 features are frequently co-located with ‘ultra-clean layers’ of depleted CCN (UHSAS100 ≤ 10
 765 cm^{-3}) in the subtropics, as seen in Figure 9b. They occur primarily at the detraining tops of
 766 cumulus clouds and are developed through collision-coalescence removal of N_d and CCN (O et
 767 al., 2018; Wood et al., 2018). The very few instances of $N_d \leq 10 \text{ cm}^{-3}$ and/or UHSAS100 ≤ 10
 768 cm^{-3} observed during SOCRATES were associated with: edges of open or cumulus-like cloud
 769 (RF02, 06), closed or stratocumulus-like cloud (RF05), or generating cells (RF03, 05); the top,
 770 often dissipating cloud layer in a multi-layer cloud (RF02, 06); and samples near snow or mixed
 771 phase precipitation (RF03, 06) (Figure S11). Although rarely sampled in SOCRATES,

772 precipitation-depleted mixed-phase cloud and aerosol features may bear future examination.
 773 These mixed-phase features are also commonly observed during the winter over the SO (Ahn et
 774 al., 2018), when FT Aitken buffering is likely less active due to reduced biological activity in the
 775 ocean.

776 N_d and near cloud CCN measured by UHSAS100 are significantly correlated at 95%
 777 confidence in both environments, with correlation coefficients $R = 0.6$ in the SO and $R = 0.76$ in
 778 the NEP (Figure 9b). As previously noted, the N_d -UHSAS100 relationship captures ACI
 779 occurring in these environments, but i) a majority of SO N_d variance is not explained, and ii) SO
 780 N_d is often higher than UHSAS100, suggesting Aitken particles are frequently activated.
 781 UHSAS100 explains more variance in N_d for CSET than SOCRATES, indicating Aitken
 782 particles are less directly important for N_d in the subtropics compared to the SO. These two
 783 regions also have significantly different amounts of SC and AC Aitken mode aerosol available: \sim
 784 200 mg^{-1} median during CSET vs. $\sim 500 \text{ mg}^{-1}$ during SOCRATES (Figure 3d, f). Supersaturation
 785 increases associated with precipitation likely occur in both regions, but the SO has a greater
 786 reservoir of MBL Aitken aerosols to prevent major N_d depletion events.

787 These lines of evidence suggest that FT Aitken aerosols act to buffer SO summertime
 788 boundary-layer clouds against precipitation depletion of N_d . A possible aerosol life cycle
 789 including the hypothesized Aitken-buffering mechanism is depicted in Figure 11 and
 790 summarized as follows:

791

- 792 I. *Marine biogenic outgassing leads to the generation of widespread high*
 793 *concentrations of small Aitken-mode aerosols in the FT via lifting, scavenging,*
 794 *and cloud outflow nucleation mechanisms (Section 3.1).*
 795 II. *Aitken-mode aerosols subside into the SO MBL through horizontal and vertical*
 796 *advection and turbulent mixing (Section 1, 3.1.1, 3.2.1).*
 797 III. *Once in the MBL, Aitken aerosols grow to accumulation mode sizes through in-*
 798 *cloud processing, coagulation, and below-cloud gas condensation (Section 1,*
 799 *3.1.3, 3.2.2).*

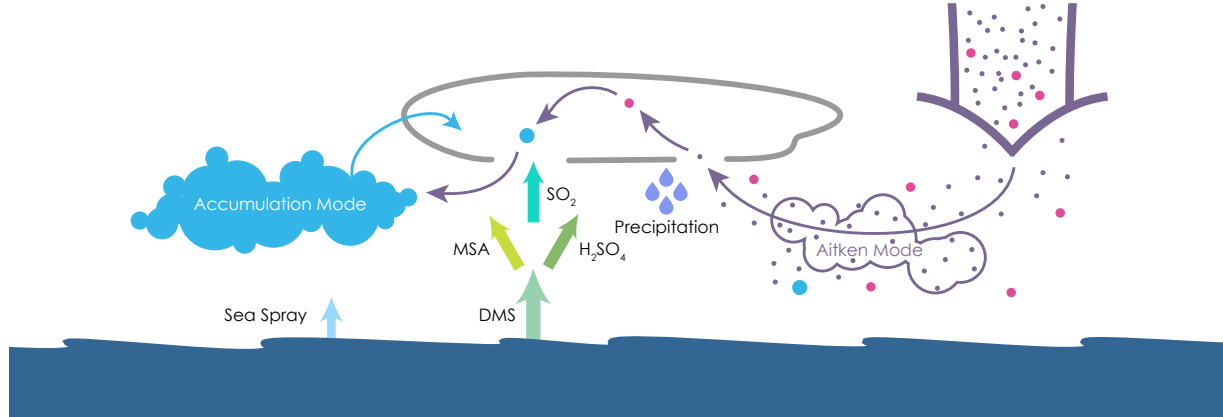
800 *Aitken-Buffering Mechanism*

- 801 IV. *SO low clouds precipitate extensively, reducing accumulation-mode aerosol*
 802 *through persistent drizzle. This leads to a reduction in boundary-layer CCN and*
 803 *an increase in peak cloud-base supersaturation.*
 804 V. *The large reservoir of Aitken aerosol in SO MBLs can be activated into CCN,*
 805 *buffering N_d against the precipitation-induced depletion commonly seen in*
 806 *subtropical MBLs.*
 807 VI. *Each activated Aitken aerosol grows by aqueous phase processing into an*
 808 *accumulation-mode aerosol, which, upon droplet evaporation, buffers the CCN-*
 809 *relevant aerosol number and reduces peak cloud-base supersaturation during*
 810 *subsequent activation events.*

811

812 This mechanism is supported by evidence presented in this paper and suggests complex
 813 interactions between aerosol and cloud processes that may not be well represented in most
 814 current climate models. Aitken-buffering over the mid-latitude oceans has the potential to reduce
 815 the frequency of precipitation-depleted cloud features, maintain cloud brightness and longevity,
 816 and reduce susceptibility to anthropogenic aerosols in general. More observational analysis and
 817 process modeling is required to better quantify Aitken influence on SO N_d characteristics.

818 Further discussion of the steps needed to test the validity of this mechanism is presented in
 819 Section 4.



820

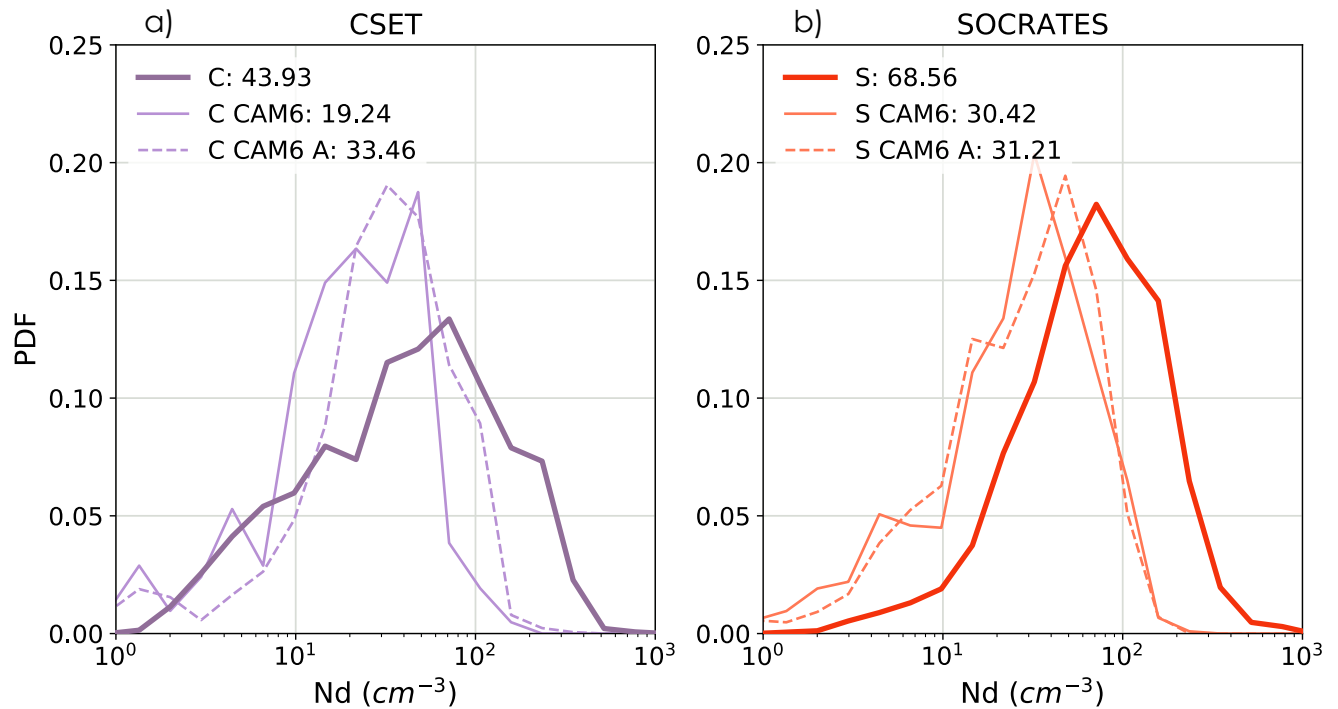
821 *Figure 11 Diagram illustrating hypothetical Aitken-buffering mechanism influencing Southern Ocean clouds. Aitken aerosol*
 822 *(subsided or entrained from the free troposphere) grow in-cloud and sub-cloud to accumulation mode sizes. Precipitation*
 823 *scavenges accumulation-mode aerosol, but this increases peak supersaturation, activating some of the large reservoir of Aitken*
 824 *aerosols to maintain CCN and N_d . This mechanism is an update and extension of aerosol life-cycles identified in the SO (Clarke*
 825 *et al., 1998; Covert et al., 1996; Quinn et al., 2017; Raes, 1995) and has important implications for aerosol-cloud interactions in*
 826 *pristine environments during biologically productive seasons.*

827 **3.3 Evaluating Southern Ocean Clouds, Aerosols, and ACI in Global Climate** 828 **Models**

829 Recent comparisons revealed that many state-of-the-art climate models under-predict N_d
 830 over the SO relative to satellite observations (Bodas-Salcedo et al., 2019; I. L. McCoy et al.,
 831 2020; Mulcahy et al., 2018; Revell et al., 2019). Identifying inconsistencies between observed
 832 and modeled cloud and aerosol characteristics will help to diagnose the underlying cause of this
 833 N_d bias. With this purpose, we compare aircraft observations from CSET and SOCRATES with
 834 meteorologically nudged CAM6 hindcasts that use prognostic aerosols and cloud droplet
 835 concentrations (Section 2.3). Examining CSET simulations allows us to determine a subtropical
 836 baseline of model ability and identify model biases unique to the SO. This nudged framework
 837 helps us to understand what mechanisms may be contributing to the current N_d bias in models
 838 and other discrepancies in ACI while ensuring that differences in the large-scale meteorology are
 839 small between the simulation and reality.

840 CAM6 consistently underpredicts N_d for both campaigns (Figure 12) and has poor
 841 correlations with co-located time-height observational composites ($R = 0.26$ for SOCRATES,
 842 none at 95% confidence for CSET, Figure S12). A confounding issue for CSET that does not
 843 significantly manifest in SOCRATES is a systematic low bias in CAM6-simulated stratocumulus
 844 cloud altitude. Thus, we include an additional comparison pdf for CAM6 in-cloud N_d averaged
 845 over all clouds in the MBL along the flight path (CAM6 A in Figure 12a) which adds context to
 846 the observationally co-located simulated N_d pdf (CAM6 in Figure 12a). CAM6 N_d for
 847 SOCRATES is less than half of observed (CAM6, CAM6 A medians of ~ 30 vs. ~ 70 cm^{-3} , a
 848 $\sim 55\%$ underestimate) while CSET has a smaller bias (CAM6 ~ 20 , CAM6 A ~ 30 vs. ~ 40 cm^{-3}
 849 observed, a ~ 55 or $\sim 25\%$ underestimate).

850

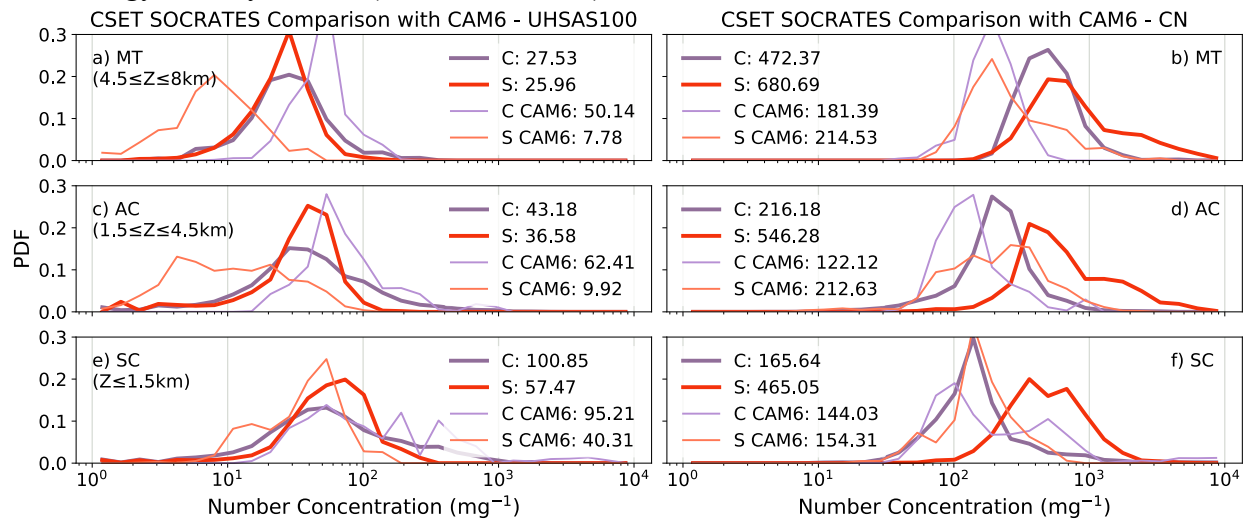


851
 852 *Figure 12 Comparison between observed and simulated N_d values during CSET (a) and SOCRATES (b). Observations and co-*
 853 *located CAM6 output for each flight during CSET and SOCRATES are binned into 50 m by 2 minute bins (Section 2.1). Data are*
 854 *restricted to $Z \leq 4$ km and at a distance from continental effects (S: south of 45°S , C: west of 130°W). Pdfs are shown for all*
 855 *observations during the campaign (solid line, same as dashed line in Figure 9c), CAM6 data that match observations temporally*
 856 *and spatially (CAM6, solid thin line), and all CAM6 data that satisfies the altitude and location criteria (i.e. not matched to*
 857 *observations) (CAM6 A, dashed line). Median values are provided.*

858 Co-located CAM6 aerosol number concentration pdfs sorted by altitude (following
 859 Figure 3) show systematic biases in CN and UHSAS100 for both campaigns (Figure 13). CAM6
 860 CSET simulations produce relatively similar SC CN and UHSAS100 pdfs (medians $\sim 15\%$ and
 861 $\sim 5\%$ underestimated, Figure 13e, f) but are more biased in the FT: underestimating CN ($\sim 45\%$
 862 AC, $\sim 60\%$ MT, Figure 13b, d) and overestimating UHSAS100 ($\sim 45\%$ AC, $\sim 80\%$ MT, Figure
 863 13a, c). CAM6 SOCRATES simulations are significantly more biased relative to observations
 864 than in the subtropics.

865 CAM6 SOCRATES CN simulations at all altitudes have a significant low bias compared
 866 to observations ($\sim 70\%$ SC and MT, $\sim 60\%$ AC, Figure 13b, d, and f). This is despite the MAM4
 867 aerosol scheme in CAM6 including a plausible mechanism for nucleating new aerosol particles
 868 from the gas phase (Liu et al., 2016). Insufficient DMS fluxes may be partly responsible for the
 869 low CN bias. CAM6 simulated monthly MT CN pdfs for SOCRATES are significantly more
 870 biased in February than in January despite similar monthly observational pdfs (underestimate of
 871 $\sim 75\%$ vs. $\sim 50\%$, Figure S13). DMS fluxes sharply decrease between January and February in the

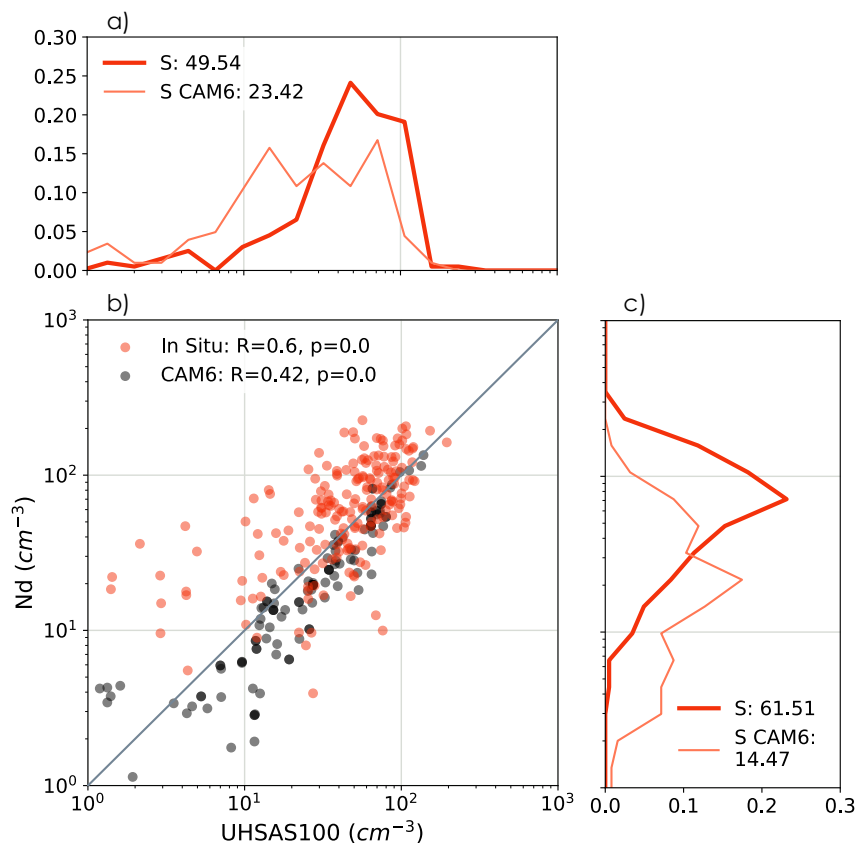
872 climatology used by CAM6 (Lana et al., 2011).



873

874 *Figure 13 As in Figure 3 but including CAM6 aerosol concentrations extracted along the flight tracks (2 min x 50 m binning, as*
 875 *in observations).*

876 CAM6 SOCRATES UHSAS100 simulations are also significantly low-biased in the FT
 877 (~70%, Figure 13a, c) with a 30% underprediction in the SC (Figure 13e). We expect this bias is
 878 inextricably linked to the significant low bias in CAM6 CN in the SO. The CAM6 UHSAS100
 879 bias manifests clearly in direct comparisons with time-height binned SOCRATES observations
 880 (~50% Figure 14a), impacting the CAM6 low bias in the ratio between UHSAS100-N_d (Figure
 881 14b) and likely the low bias in matched N_d (~75%, Figure 14c).



882

883 *Figure 14 Relationship between SOCRATES accumulation mode and cloud droplet number concentrations as in Figure 9 but*
 884 *including CAM6 collocated to observations (binned into 50 m by 2 minute bins) for each flight (black in b; thin, light orange line*
 885 *in a, c) in addition to observations (orange in b; thick, dark orange line in a, c). Pdfs of number concentrations for matched*
 886 *binned values occurring for CAM6 and observations are shown with median values for UHSAS100 (a) and N_d (c). Scatters of*
 887 *UHSAS100 against N_d (b) are shown along with the correlation coefficients and p-values for in-situ and CAM6 relationships.*
 888 *Data are restricted to $Z \leq 4$ km and in pristine regions south of 45°S .*

889 There are several implications from this model-observation comparison for the issues
 890 challenging CAM6's ability to simulate the SO and other pristine environments:

- 891 i. Physical mechanisms relevant to generating Aitken aerosols from DMS-oxidation
 892 products (which we expect to dominate SO CN) while included in CAM6 (Liu et
 893 al., 2016) may be insufficient. CAM6 simulated CN pdfs are both systematically
 894 too low at all altitudes in the SO and strikingly similar for CSET and SOCRATES
 895 despite the large differences in the observational pdfs and environments for these
 896 two campaigns (Figure 13b, d, and f). Even when more DMS is available in the
 897 SO (January), high CN concentrations linked to RPF are under-produced (Figure
 898 S13). Mechanism discrepancies associated with cloud-outflow particle formation
 899 may also lead to the low biased MT CN during CSET (Figure 13b).
- 900 ii. Low biases in FT Aitken aerosol (Figure 13b, d) result in insufficient entrainment
 901 of particles into the MBL in CAM6 (low biased SC CN, Figure 13f), drastically
 902 limiting the ability for FT Aitken aerosol to grow into the main CCN source in the
 903 SO summertime (Section 3.2.2, e.g. (Covert et al., 1996; Korhonen et al., 2008;
 904 Quinn et al., 2017; Raes, 1995)). This would influence other regions where FT

905 Aitken aerosol is a prominent SC CCN source (e.g. in the northeast Atlantic
 906 (Sanchez et al., 2018; Zheng et al., 2018)).
 907 iii. Over-production of sea-spray aerosol in CAM6 may compensate on average for
 908 low biases in sulfur-based accumulation mode aerosol concentrations connected
 909 to low biases in Aitken aerosols in MBL SO summertime. Compared to
 910 SOCRATES observations, CAM6 UHSAS100 is 30% lower SC (Figure 13) and
 911 50% lower near-cloud (Figure 14a, b) but CAM6 CN is 70% lower SC (Figure
 912 13f). This suggests significant surface aerosol contributions to accumulation mode
 913 number in CAM6, likely from sea-spray mechanisms, which is inconsistent with
 914 observations (Section 3.1.3, 3.2.2) but similar to biases found in other state-of-
 915 the-art climate models (Revell et al., 2019).

916
 917 CAM6 simulations of SO low clouds are generally fairly skillful (Gettelman et al., 2020;
 918 Zhou et al., 2020) but there are some significant cloud-regime specific biases that may also
 919 impact simulated SO N_d and should be addressed after the more prescient aerosol biases are
 920 resolved. Cloud droplet concentration is affected by an especially complex balance between
 921 aerosol sources and sinks (Wood et al., 2012) and the SO is no exception (I. L. McCoy et al.,
 922 2020). Precipitation, the major sink, has been overly-active in the SO in past GCMs (Stephens et
 923 al., 2010). While precipitation bias is small on average for SOCRATES CAM6 simulations,
 924 precipitation is over-produced in cumulus-like clouds and under-produced in stratocumulus
 925 clouds (Zhou et al., 2020). CAM6 phase partitioning, particularly production of super-cooled
 926 liquid clouds, shows little bias across the campaign (Gettelman et al., 2020; Zhou et al., 2020)
 927 but cumulus clouds are excessively glaciated (Atlas et al., 2020). Activation of CCN into N_d is
 928 dependent on CCN availability (which we show in this paper has a campaign-wide bias) and
 929 turbulent updrafts. CAM6 turbulence agrees with observations in unstable regimes but is under-
 930 produced in stable and neutral MBLs (Atlas et al., 2020). Thus, it is likely that in addition to the
 931 significant aerosol biases in CAM6, there may be compensating, cloud-regime specific biases
 932 between precipitation, glaciation, turbulence and activation that make teasing out the underlying
 933 causes of the N_d bias difficult.

934

935 4 Discussion

936 SOCRATES observations both confirm and expand upon earlier studies in the SO. The
 937 summertime N_d sampled by SOCRATES (median $\sim 70 \text{ cm}^{-3}$, Figure 9c) is significantly higher
 938 than average MBL N_d sampled in the austral winter slightly to the north of this region (mean \sim
 939 30 cm^{-3} between 43-45°S) (Ahn et al., 2018). This seasonality is consistent with earlier work
 940 linking N_d increases to increased availability of DMS products and aerosol sourced from ocean
 941 biology in the SO summertime (Ayers & Gras, 1991; Boers et al., 1998; Charlson et al., 1987; D.
 942 T. McCoy et al., 2015; I. L. McCoy et al., 2020).

943 Entrainment and subsidence of FT Aitken particles into the MBL (Covert et al., 1996;
 944 Humphries et al., 2016; Sanchez et al., 2021; Schmale et al., 2019) and its central importance as
 945 a source for MBL CCN in the SO (Covert et al., 1996; Korhonen et al., 2008; Raes, 1995;
 946 Sanchez et al., 2021; Schmale et al., 2019), the NEA (Sanchez et al., 2018; Zheng et al., 2018),
 947 and generally between 70°S and 80°N (Quinn et al., 2017) have been previously established.
 948 SOCRATES observations of aerosol composition, vertical concentration profiles, and co-located

949 cloud properties further cements the importance of FT Aitken aerosol influence on SO SC CCN
950 and N_d .

951 The hypothesized aerosol lifecycle involving the Aitken-buffering mechanism (e.g.
952 synoptic lofting of DMS, particle generation in the FT from DMS-oxidation products, Aitken
953 particle descent into the MBL, Aitken particle growth into accumulation mode sizes below
954 cloud, and increased activation of Aitken particles in response to precipitation depletion) would
955 require large spatial scales. This is consistent with stronger correlations found between DMS
956 fluxes and N_d over large spatial scales (Andreae et al., 1995; Covert et al., 1996; D. T. McCoy et
957 al., 2015) and limited local correlations (Covert et al., 1996).

958 Future examination of the impact of the Aitken-buffering mechanism on the SO and other
959 pristine environments is needed. The Aitken-buffering mechanism may influence other pristine
960 biologically productive marine regions (e.g. the northeast Atlantic (Sanchez et al., 2018; Zheng
961 et al., 2018)), especially given the importance of entrained FT aerosol on CCN globally (Quinn
962 et al., 2017). The influence of this mechanism should be considered in evaluating the
963 susceptibility of pristine clouds to anthropogenic aerosol (Carslaw et al., 2013) and in
964 constraining radiative forcing associated with ACI (Bellouin et al., 2020; I. L. McCoy et al.,
965 2020; Regayre et al., 2019). The feasibility of entrained FT Aitken particles buffering the CCN
966 budget will be determined by the balance between the rate of precipitation depletion of N_d
967 compared to the rate of Aitken mode activation and growth to cloud affecting sizes. This time
968 scale, as well as general mechanism robustness, could be examined using aerosol-coupled large
969 eddy simulations supported by SO aerosol and cloud observations but would not be easily
970 observable alone. Future examinations should also address the role of mixed-phase and super-
971 cooled cloud physics on SO ACI, impacting the generalizability of the Aitken-buffering
972 mechanism to other pristine environments. How the presence of giant CCN (Jensen & Nugent,
973 2017) in the SO (McFarquhar et al., 2020) influences supersaturation changes, and subsequent
974 Aitken activation, in response to precipitation removal is also worth examining.

975 Additional observations contrasting biologically active (summer) and inactive (winter)
976 seasons in the SO can help us to further document ACI in this region. It is critical that future SO
977 aircraft campaigns capture Aitken as well as accumulation mode size distributions and
978 concurrently measure aerosol composition and trace gas species (e.g. DMS, H_2SO_4 , and MSA),
979 and how they vary with altitude and boundary-layer regime. Measurements of DMS and
980 precursor gases at the surface and aloft would enable rate calculations and estimates of
981 processing time for aerosol formation, growth, and depletion as well as an estimation of the
982 degree of long-range influence phytoplankton can exert on SO clouds and aerosols.

983 This paper illustrates some of the complexities of SO aerosol production and growth and
984 underlines the importance of understanding and representing these mechanisms in GCMs.
985 Simulating both mechanisms highlighted in this paper (FT Aitken production through synoptic-
986 uplift and Aitken-buffering in the MBL) requires a good model of relevant marine biogenic
987 emissions. However, neglecting natural new particle formation in GCMs leads to overestimation
988 in the magnitude of the radiative forcing associated with ACI (Gordon et al., 2017). Thus,
989 inclusion of these mechanisms will likely advance the simulation of SO ACI and reduce
990 associated radiative biases, further constraining radiative forcing associated with ACI (Bodas-
991 Salcedo et al., 2019; I. L. McCoy et al., 2020; Regayre et al., 2019).

992 5 Summary

993 Observations from the 2018 SOCRATES campaign suggest that new particle formation is
 994 widespread and frequent in the summertime Southern Ocean free troposphere (FT, 3-6 km) and
 995 dominates the aerosol characteristics of that region. Typical observed signatures of recent
 996 particle formation (RPF) events included high and rapidly varying concentrations of total aerosol
 997 number concentrations (diameters $\geq 0.011 \mu\text{m}$, $\text{CN} \geq 1000 \text{ mg}^{-1}$), low accumulation and coarse
 998 mode aerosol surface area (diameters $0.1\text{-}50 \mu\text{m}$, $\text{SA} \leq 10 \mu\text{m}^2 \text{ mg}^{-1}$), and low accumulation-
 999 mode aerosol number concentrations (diameters $0.1\text{-}1 \mu\text{m}$, $\text{UHSAS100} \leq 80 \text{ mg}^{-1}$). FT Aitken
 1000 mode particles (diameters $\leq 0.1 \mu\text{m}$) showed volatility signatures of H_2SO_4 or more volatile
 1001 DMS-oxidation products.

1002 Back-trajectory analysis of RPF classified events ($\text{CN} \geq 2500 \text{ mg}^{-1}$) showed air masses
 1003 had recently ascended from below 1 km to the FT at synoptic rates ($w \geq 1 \text{ cm s}^{-1}$). Warm-
 1004 conveyor belts and sub-polar vortices were the two main synoptic drivers of this ascent seen in
 1005 the SO FT. Broadly, these RPF events are described by a synoptic uplift mechanism for particle
 1006 generation: boundary-layer air parcels rich in marine biogenic gases (i.e. DMS) are swept up via
 1007 synoptic motions through cloud, precipitation scavenges large aerosols and reduces aerosol SA,
 1008 and gas-to-particle conversion occurs in the FT upon cloud exit once DMS oxidizes into
 1009 precursor gases (e.g. SO_2 , H_2SO_4 , and MSA). This proposed mechanism explains the prevalence
 1010 and high concentration of FT Aitken aerosols observed over the SO by SOCRATES, works in
 1011 concert with other cloud outflow particle formation mechanisms occurring at lower altitudes in
 1012 the SO (Clarke et al., 1998), and will be active mainly in summer since outgassing of DMS from
 1013 a biologically active ocean is essential.

1014 Aitken-mode aerosol concentrations are nearly as high in the summertime SO MBL as in
 1015 the FT and substantially higher than in remote parts of the marine subtropics (i.e. the CSET
 1016 campaign in the northeast Pacific). Sub-cloud aerosol distributions and correlations with wind
 1017 speed corroborate earlier work showing sea spray aerosol does not control CCN number over the
 1018 summertime SO (e.g. Quinn et al. (2017)). Instead, patterns of aerosol number concentrations,
 1019 size distributions, and compositions (Twohy et al., 2021) support the dominant source of sub-
 1020 cloud CCN and driver of SO N_d is entrainment and subsequent growth of Aitken aerosol from the
 1021 large FT reservoir (e.g. (Bates et al., 1998; Covert et al., 1996; Humphries et al., 2016; Korhonen
 1022 et al., 2008; Quinn et al., 2017; Raes, 1995)).

1023 After entraining into the MBL, the high SO concentrations of Aitken aerosol may buffer
 1024 N_d and CCN against the effects of precipitation. Precipitation scavenging activates more MBL
 1025 Aitken aerosol (continuously sourced from the FT and grown within the MBL) to combat this
 1026 sink of accumulation-mode aerosol and resist depletion of N_d . Lack of precipitation-depleted
 1027 cloud features during SOCRATES and consistently high N_d in the SO despite a significant
 1028 precipitation sink (I. L. McCoy et al., 2020) are evidence for this hypothesized Aitken-buffering
 1029 mechanism. Observations from the subtropical northeast Pacific, where Aitken concentrations
 1030 just above and within the MBL are much lower than in the SO, show contrasting behavior (e.g.
 1031 frequent precipitation-depleted cloud features).

1032 Meteorologically nudged CAM6 simulations for SOCRATES show significant low
 1033 biases in N_d ; free tropospheric, near cloud, and (to a lesser extent) sub-cloud accumulation mode
 1034 aerosol; and Aitken mode aerosol concentrations at all altitudes in the SO. Over-production of
 1035 sea-spray aerosol at the surface (e.g. Revell et al. (2019)) may mask accumulation mode bias in
 1036 CAM6 associated with insufficient FT Aitken aerosol production and subsequent entrainment
 1037 into the SO MBL, where it is essential for growing sulfur-based CCN. Simulated SO and

1038 subtropical aerosol behavior are extremely similar despite large regional differences in the real
 1039 world. We conclude that while CAM6 includes simplified representations of the aerosol, cloud,
 1040 and marine biogenic emission processes — whose importance we highlight in this paper —
 1041 further improvements must be made in CAM6 to achieve quantitative accuracy in simulating the
 1042 aerosol-cloud interactions and typical, seasonally-varying range of N_d over the summertime SO.
 1043 SO N_d biases in other state-of-the-art climate models suggest they also need such improvements
 1044 in simulating pristine environments, which can be informed by detailed SO field studies such as
 1045 SOCRATES (Bodas-Salcedo et al., 2019; I. L. McCoy et al., 2020; Revell et al., 2019)).
 1046

1047 **Acknowledgments**

1048 The authors wish to thank Mike Reeves for help in interpreting aerosol observations. They
 1049 further thank Rachel Atlas, Cristina McCluskey, Matt Wyant, Roger Marchand, Xiaoli Zhou,
 1050 Litai Kang, Kevin Sanchez, and the SOCRATES team for productive discussions of this work.

1051 The National Science Foundation supports the SOCRATES campaign and its continued research
 1052 efforts (AGS-1660609). Additionally, CHT acknowledges funding through grant AGS-1660605.

1053 ILM, CSB, and RW developed scientific hypothesis, method of approach, and wrote the paper.
 1054 ILM obtained and analyzed data, ran HYSPLIT trajectories, and extracted model data to match
 1055 observations. CHT and DWT helped to interpret volatility estimates. AG and CB supplied
 1056 CAM6 nudged simulations for CSET and SOCRATES. All authors contributed to writing and
 1057 editing the paper.

1058 **Data Availability**

1059 NCAR EOL provided aircraft data from the SOCRATES campaign (UCAR/NCAR, 2019) and
 1060 CSET campaign (UCAR/NCAR, 2017). All information and datasets can be found through the
 1061 supporting EOL websites (https://www.eol.ucar.edu/field_projects/socrates and
 1062 <http://catalog.eol.ucar.edu/cset>). HYSPLIT Back Trajectories were calculated from SOCRATES
 1063 positions using the publicly available HYSPLIT code
 1064 (<https://www.ready.noaa.gov/HYSPLIT.php>). ERA5 Reanalysis products are accessible through
 1065 the online database at ECMWF ([https://www.ecmwf.int/en/forecasts/datasets/reanalysis-](https://www.ecmwf.int/en/forecasts/datasets/reanalysis-datasets/era5)
 1066 [datasets/era5](https://www.ecmwf.int/en/forecasts/datasets/reanalysis-datasets/era5)). CAM6 simulations for SOCRATES and CSET are available online at
 1067 <https://doi.org/10.5281/zenodo.4480387> (I. L. McCoy et al., 2021).
 1068

1069 **References**

- 1070
 1071 Ahn, E., Huang, Y., Siems, S. T., & Manton, M. J. (2018). A Comparison of Cloud Microphysical Properties
 1072 Derived From MODIS and CALIPSO With In Situ Measurements Over the Wintertime Southern Ocean.
 1073 *Journal of Geophysical Research: Atmospheres*, 123(19), 11,120-111,140. <Go to
 1074 ISI>://WOS:000448374800020
- 1075 Albrecht, B., Ghate, V., Mohrmann, J., Wood, R., Zuidema, P., Bretherton, C., et al. (2019). Cloud System
 1076 Evolution in the Trades-CSET: Following the Evolution of Boundary Layer Cloud Systems with the
 1077 NSF/NCAR GV. *Bull Am Meteorol Soc*, 100(1), 93-121. <https://www.ncbi.nlm.nih.gov/pubmed/32042201>

- 1078 Andreae, M. O., Elbert, W., & de Mora, S. J. (1995). Biogenic sulfur emissions and aerosols over the tropical South
 1079 Atlantic: 3. Atmospheric dimethylsulfide, aerosols and cloud condensation nuclei. *Journal of Geophysical*
 1080 *Research*, 100(D6), 11335-11356. <Go to ISI>://WOS:A1995RF05100024
- 1081 Andreae, M. O., Jones, C. D., & Cox, P. M. (2005). Strong present-day aerosol cooling implies a hot future. *Nature*,
 1082 435(7046), 1187-1190. Article. <https://www.ncbi.nlm.nih.gov/pubmed/15988515>
- 1083 Atlas, R. L., Bretherton, C. S., Blosssey, P. N., Gettelman, A., Bardeen, C., Lin, P., & Ming, Y. (2020). How Well
 1084 Do Large-Eddy Simulations and Global Climate Models Represent Observed Boundary Layer Structures
 1085 and Low Clouds Over the Summertime Southern Ocean? *Journal of Advances in Modeling Earth Systems*,
 1086 12(11).
- 1087 Ayers, G. P., Caine, J. M., Gillett, R. W., & Ivey, J. P. (1997). Atmospheric sulphur and cloud condensation nuclei
 1088 in marine air in the Southern Hemisphere. *Philosophical Transactions of the Royal Society of London*
 1089 *Series B-Biological Sciences*, 352(1350), 203-211. <Go to ISI>://WOS:A1997WM31700014
- 1090 Ayers, G. P., & Gillett, R. W. (2000). DMS and its oxidation products in the remote marine atmosphere:
 1091 implications for climate and atmospheric chemistry. *Journal of Sea Research*, 43(3-4), 275-286. <Go to
 1092 ISI>://WOS:000089555600011
- 1093 Ayers, G. P., & Gras, J. L. (1991). Seasonal relationship between cloud condensation nuclei and aerosol
 1094 methanesulphonate in marine air. *Nature*, 353(6347), 834-835. <Go to ISI>://WOS:A1991GM73200055
 1095 <http://www.nature.com/nature/journal/v353/n6347/pdf/353834a0.pdf>
- 1096 Bates, T. S. (2002). Regional marine boundary layer aerosol size distributions in the Indian, Atlantic, and Pacific
 1097 Oceans: A comparison of INDOEX measurements with ACE-1, ACE-2, and Aerosols99. *Journal of*
 1098 *Geophysical Research*, 107(D19), INX2 25-21-INX22 25-15.
 1099 <https://agupubs.onlinelibrary.wiley.com/doi/abs/10.1029/2001JD001174>
- 1100 Bates, T. S., Kapustin, V. N., Quinn, P. K., Covert, D. S., Coffman, D. J., Mari, C., et al. (1998). Processes
 1101 controlling the distribution of aerosol particles in the lower marine boundary layer during the First Aerosol
 1102 Characterization Experiment (ACE 1). *Journal of Geophysical Research: Atmospheres*, 103(D13), 16369-
 1103 16383.
- 1104 Bellouin, N., Quaas, J., Gryspeerdt, E., Kinne, S., Stier, P., Watson-Parris, D., et al. (2020). Bounding Global
 1105 Aerosol Radiative Forcing of Climate Change. *Rev Geophys*, 58(1), e2019RG000660.
 1106 <https://www.ncbi.nlm.nih.gov/pubmed/32734279>
- 1107 Berresheim, H., Elste, T., Tremmel, H. G., Allen, A. G., Hansson, H.-C., Rosman, K., et al. (2002). Gas-aerosol
 1108 relationships of H₂SO₄, MSA, and OH: Observations in the coastal marine boundary layer at Mace Head,
 1109 Ireland. *Journal of Geophysical Research*, 107(D19). <Go to ISI>://WOS:000180428300008
- 1110 Bigg, E. K. (2007). Sources, nature and influence on climate of marine airborne particles. *Environmental Chemistry*,
 1111 4(3), 155-161. <Go to ISI>://WOS:000247436800004
- 1112 Bigg, E. K., & Leck, C. (2008). The composition of fragments of bubbles bursting at the ocean surface. *Journal of*
 1113 *Geophysical Research*, 113(D11). <Go to ISI>://WOS:000256811300002
- 1114 Bodas-Salcedo, A., Hill, P. G., Furtado, K., Williams, K. D., Field, P. R., Manners, J. C., et al. (2016). Large
 1115 Contribution of Supercooled Liquid Clouds to the Solar Radiation Budget of the Southern Ocean. *Journal*
 1116 *of Climate*, 29(11), 4213-4228. <Go to ISI>://WOS:000377116500003
- 1117 Bodas-Salcedo, A., Mulcahy, J. P., Andrews, T., Williams, K. D., Ringer, M. A., Field, P. R., & Elsaesser, G. S.
 1118 (2019). Strong Dependence of Atmospheric Feedbacks on Mixed-Phase Microphysics and Aerosol-Cloud

- 1119 Interactions in HadGEM3. *J Adv Model Earth Syst*, 11(6), 1735-1758.
 1120 <https://www.ncbi.nlm.nih.gov/pubmed/31598189>
- 1121 Bodas-Salcedo, A., Williams, K. D., Field, P. R., & Lock, A. P. (2012). The Surface Downwelling Solar Radiation
 1122 Surplus over the Southern Ocean in the Met Office Model: The Role of Midlatitude Cyclone Clouds.
 1123 *Journal of Climate*, 25(21), 7467-7486. Article. <Go to ISI>://WOS:000311002700009
- 1124 Bodas-Salcedo, A., Williams, K. D., Ringer, M. A., Beau, I., Cole, J. N. S., Dufresne, J. L., et al. (2014). Origins of
 1125 the Solar Radiation Biases over the Southern Ocean in CFMIP2 Models*. *Journal of Climate*, 27(1), 41-56.
 1126 Article. <Go to ISI>://WOS:000329276000003
- 1127 Boers, R., Jensen, J. B., & Krummel, P. B. (1998). Microphysical and short-wave radiative structure of
 1128 stratocumulus clouds over the Southern Ocean: Summer results and seasonal differences. *Quarterly*
 1129 *Journal of the Royal Meteorological Society*, 124(545), 151-168. <Go to ISI>://WOS:000072056700006
- 1130 Bretherton, C. S., McCoy, I. L., Mohrmann, J., Wood, R., Ghate, V., Gettelman, A., et al. (2019). Cloud, Aerosol,
 1131 and Boundary Layer Structure across the Northeast Pacific Stratocumulus?Cumulus Transition as Observed
 1132 during CSET. *Monthly Weather Review*, 147(6), 2083-2103.
 1133 <https://journals.ametsoc.org/view/journals/mwrc/147/6/mwr-d-18-0281.1.xml>
- 1134 Carslaw, K. S., Lee, L. A., Reddington, C. L., Pringle, K. J., Rap, A., Forster, P. M., et al. (2013). Large contribution
 1135 of natural aerosols to uncertainty in indirect forcing. *Nature*, 503(7474), 67-71. Article.
 1136 <https://www.ncbi.nlm.nih.gov/pubmed/24201280>
- 1137 Catto, J. L., Madonna, E., Joos, H., Rudeva, I., & Simmonds, I. (2015). Global Relationship between Fronts and
 1138 Warm Conveyor Belts and the Impact on Extreme Precipitation*. *Journal of Climate*, 28(21), 8411-8429.
 1139 <Go to ISI>://WOS:000363766200007
- 1140 Chand, D., Wood, R., Ghan, S. J., Wang, M., Ovchinnikov, M., Rasch, P. J., et al. (2012). Aerosol optical depth
 1141 increase in partly cloudy conditions. *Journal of Geophysical Research: Atmospheres*, 117(D17), n/a-n/a.
 1142 <Go to ISI>://WOS:000308892800003
- 1143 Chandrakar, K. K., Cantrell, W., Ciochetto, D., Karki, S., Kinney, G., & Shaw, R. A. (2017). Aerosol removal and
 1144 cloud collapse accelerated by supersaturation fluctuations in turbulence. *Geophysical Research Letters*,
 1145 44(9), 4359-4367. <Go to ISI>://WOS:000402143700047
- 1146 Charlson, R. J., Lovelock, J. E., Andreae, M. O., & Warren, S. G. (1987). Oceanic phytoplankton, atmospheric
 1147 sulphur, cloud albedo and climate. *Nature*, 326(6114), 655-661. Review. <Go to
 1148 ISI>://WOS:A1987G890600046
- 1149 Clarke, A. D. (1991). A thermo-optic technique for in situ analysis of size-resolved aerosol physicochemistry.
 1150 *Atmospheric Environment. Part A. General Topics*, 25(3-4), 635-644.
 1151 <http://www.sciencedirect.com/science/article/pii/096016869190061B>
- 1152 Clarke, A. D. (1993). Atmospheric nuclei in the Pacific midtroposphere: Their nature, concentration, and evolution.
 1153 *Journal of Geophysical Research*, 98(D11), 20633-20647. <Go to ISI>://WOS:A1993MJ29800026
- 1154 Clarke, A. D., Ahlquist, N. C., & Covert, D. S. (1987). The Pacific marine aerosol: Evidence for natural acid
 1155 sulfates. *Journal of Geophysical Research: Atmospheres*, 92(D4), 4179-4190.
 1156 <https://agupubs.onlinelibrary.wiley.com/doi/abs/10.1029/JD092iD04p04179>
- 1157 Clarke, A. D., Varner, J. L., Eisele, F., Mauldin, R. L., Tanner, D., & Litchy, M. (1998). Particle production in the
 1158 remote marine atmosphere: Cloud outflow and subsidence during ACE 1. *Journal of Geophysical*
 1159 *Research: Atmospheres*, 103(D13), 16397-16409. <Go to ISI>://WOS:000074828200032

- 1160 Clement, C. F., Ford, I. J., Twohy, C. H., Weinheimer, A., & Campos, T. (2002). Particle production in the outflow
 1161 of a midlatitude storm. *Journal of Geophysical Research: Atmospheres*, 107(D21), AAC 5-1-AAC 5-9.
 1162 <Go to ISI>://WOS:000180860300011
- 1163 Covert, D. S., Kapustin, V. N., Bates, T. S., & Quinn, P. K. (1996). Physical properties of marine boundary layer
 1164 aerosol particles of the mid-Pacific in relation to sources and meteorological transport. *Journal of*
 1165 *Geophysical Research: Atmospheres*, 101(D3), 6919-6930. <Go to ISI>://WOS:A1996UB98600018
- 1166 Dunne, E. M., Gordon, H., Kurten, A., Almeida, J., Duplissy, J., Williamson, C., et al. (2016). Global atmospheric
 1167 particle formation from CERN CLOUD measurements. *Science*, 354(6316), 1119-1124.
 1168 <https://www.ncbi.nlm.nih.gov/pubmed/27789796>
- 1169 Eckhardt, S., Stohl, A., Wernli, H., James, P., Forster, C., & Spichtinger, N. (2004). A 15-Year Climatology of
 1170 Warm Conveyor Belts. *Journal of Climate*, 17(1), 218-237. <Go to ISI>://WOS:000187742400016
- 1171 Fitzgerald, J. W. (1991). Marine aerosols: A review. *Atmospheric Environment. Part A. General Topics*, 25(3-4),
 1172 533-545. <Go to ISI>://WOS:A1991FF35800002
- 1173 Forster, P. M. (2016). Inference of Climate Sensitivity from Analysis of Earth's Energy Budget. *Annual Review of*
 1174 *Earth and Planetary Sciences*, 44(1), 85-106. <Go to ISI>://WOS:000379329700005
- 1175 Fossum, K. N., Ovadnevaite, J., Ceburnis, D., Dall'Osto, M., Marullo, S., Bellacicco, M., et al. (2018). Summertime
 1176 Primary and Secondary Contributions to Southern Ocean Cloud Condensation Nuclei. *Scientific Reports*,
 1177 8(1), 13844. <https://www.ncbi.nlm.nih.gov/pubmed/30218089>
- 1178 Gelaro, R., McCarty, W., Suarez, M. J., Todling, R., Molod, A., Takacs, L., et al. (2017). The Modern-Era
 1179 Retrospective Analysis for Research and Applications, Version 2 (MERRA-2). *J Clim, Volume 30*(Iss 13),
 1180 5419-5454. <https://www.ncbi.nlm.nih.gov/pubmed/32020988>
- 1181 Gettelman, A., Bardeen, C. G., McCluskey, C. S., Järvinen, E., Stith, J., Bretherton, C., et al. (2020). Simulating
 1182 Observations of Southern Ocean Clouds and Implications for Climate. *Journal of Geophysical Research:*
 1183 *Atmospheres*, 125(21). <Go to ISI>://WOS:000591896900002
 1184 <https://agupubs.onlinelibrary.wiley.com/doi/10.1029/2020JD032619>
- 1185 Gordon, H., Kirkby, J., Baltensperger, U., Bianchi, F., Breitenlechner, M., Curtius, J., et al. (2017). Causes and
 1186 importance of new particle formation in the present-day and preindustrial atmospheres. *Journal of*
 1187 *Geophysical Research: Atmospheres*, 122(16), 8739-8760. <Go to ISI>://WOS:000416382800021
- 1188 Grosvenor, D. P., Sourdeval, O., Zuidema, P., Ackerman, A., Alexandrov, M. D., Bennartz, R., et al. (2018).
 1189 Remote Sensing of Droplet Number Concentration in Warm Clouds: A Review of the Current State of
 1190 Knowledge and Perspectives. *Rev Geophys*, 56(2), 409-453.
 1191 <https://www.ncbi.nlm.nih.gov/pubmed/30148283>
- 1192 Grythe, H., Ström, J., Krejci, R., Quinn, P., & Stohl, A. (2014). A review of sea-spray aerosol source functions using
 1193 a large global set of sea salt aerosol concentration measurements. *Atmospheric Chemistry and Physics*,
 1194 14(3), 1277-1297. <Go to ISI>://WOS:000332384900009
- 1195 Hamilton, D. S., Lee, L. A., Pringle, K. J., Reddington, C. L., Spracklen, D. V., & Carslaw, K. S. (2014).
 1196 Occurrence of pristine aerosol environments on a polluted planet. *Proc Natl Acad Sci U S A*, 111(52),
 1197 18466-18471. Article. <https://www.ncbi.nlm.nih.gov/pubmed/25512511>
- 1198 Hobbs, P. V. (1971). Simultaneous airborne measurements of cloud condensation nuclei and sodium-containing
 1199 particles over the ocean. *Quarterly Journal of the Royal Meteorological Society*, 097(413), 263-271. <Go
 1200 to ISI>://WOS:A1971K009800001

- 1201 Hodshire, A. L., Campuzano-Jost, P., Kodros, J. K., Croft, B., Nault, B. A., Schroder, J. C., et al. (2019). The
 1202 potential role of methanesulfonic acid (MSA) in aerosol formation and growth and the associated radiative
 1203 forcings. *Atmospheric Chemistry and Physics*, 19(5), 3137-3160. <Go to ISI>://WOS:000460947700002
- 1204 Holton, J. R., & Haikm, G. J. (2013). *An Introduction to Dynamic Meteorology* (Fifth ed.). Academic Press:
 1205 Elsevier.
- 1206 Humphries, R. S., Klekociuk, A. R., Schofield, R., Keywood, M., Ward, J., & Wilson, S. R. (2016). Unexpectedly
 1207 high ultrafine aerosol concentrations above East Antarctic sea ice. *Atmospheric Chemistry and Physics*,
 1208 16(4), 2185-2206. <Go to ISI>://WOS:000372971500021
- 1209 Jennings, S. G., & O'Dowd, C. D. (1990). Volatility of aerosol at Mace Head, on the west coast of Ireland. *Journal*
 1210 *of Geophysical Research: Atmospheres*, 95(D9), 13937-13948.
 1211 <https://agupubs.onlinelibrary.wiley.com/doi/abs/10.1029/JD095iD09p13937>
- 1212 Jennings, S. G., O'Dowd, C. D., Cooke, W. F., Sheridan, P. J., & Cachier, H. (1994). Volatility of elemental carbon.
 1213 *Geophysical Research Letters*, 21(16), 1719-1722.
 1214 <https://agupubs.onlinelibrary.wiley.com/doi/abs/10.1029/94GL01423>
- 1215 Jensen, J. B., & Nugent, A. D. (2017). Condensational Growth of Drops Formed on Giant Sea-Salt Aerosol
 1216 Particles. *Journal of the Atmospheric Sciences*, 74(3), 679-697.
- 1217 Kang, L., Marchand, R. T., & Smith, W. L. (2021). Evaluation of MODIS and Himawari-8 Low Clouds Retrievals
 1218 over the Southern Ocean with In Situ Measurements from the SOCRATES Campaign. *Earth and Space*
 1219 *Science*, n/a(n/a), e2020EA001397.
 1220 <https://agupubs.onlinelibrary.wiley.com/doi/abs/10.1029/2020EA001397>
- 1221 Kaufman, Y. J., & Tanré, D. (1994). Effect of variations in super-saturation on the formation of cloud condensation
 1222 nuclei. *Nature*, 369(6475), 45-48. <https://doi.org/10.1038/369045a0>
- 1223 Kazil, J., Wang, H., Feingold, G., Clarke, A. D., Snider, J. R., & Bandy, A. R. (2011). Modeling chemical and
 1224 aerosol processes in the transition from closed to open cells during VOCALS-REx. *Atmospheric Chemistry*
 1225 *and Physics*, 11(15), 7491-7514. Article. <Go to ISI>://WOS:000293826500006
- 1226 Kerminen, V.-M., Chen, X., Vakkari, V., Petäjä, T., Kulmala, M., & Bianchi, F. (2018). Atmospheric new particle
 1227 formation and growth: review of field observations. *Environmental Research Letters*, 13(10). <Go to
 1228 ISI>://WOS:000445933100002
- 1229 Kirkby, J., Curtius, J., Almeida, J., Dunne, E., Duplissy, J., Ehrhart, S., et al. (2011). Role of sulphuric acid,
 1230 ammonia and galactic cosmic rays in atmospheric aerosol nucleation. *Nature*, 476(7361), 429-433.
 1231 <https://www.ncbi.nlm.nih.gov/pubmed/21866156>
- 1232 Korhonen, H., Carslaw, K. S., Spracklen, D. V., Mann, G. W., & Woodhouse, M. T. (2008). Influence of oceanic
 1233 dimethyl sulfide emissions on cloud condensation nuclei concentrations and seasonality over the remote
 1234 Southern Hemisphere oceans: A global model study. *Journal of Geophysical Research*, 113(D15). <Go to
 1235 ISI>://WOS:000258339000004
- 1236 Kupc, A., Williamson, C., Wagner, N. L., Richardson, M., & Brock, C. A. (2018). Modification, calibration, and
 1237 performance of the Ultra-High Sensitivity Aerosol Spectrometer for particle size distribution and volatility
 1238 measurements during the Atmospheric Tomography Mission (ATom) airborne campaign. *Atmospheric*
 1239 *Measurement Techniques*, 11(1), 369-383. <Go to ISI>://WOS:000422881100002
- 1240 Kürten, A., Bianchi, F., Almeida, J., Kupiainen-Määttä, O., Dunne, E. M., Duplissy, J., et al. (2016). Experimental
 1241 particle formation rates spanning tropospheric sulfuric acid and ammonia abundances, ion production rates,
 1242 and temperatures. *Journal of Geophysical Research: Atmospheres*, 121(20).

- 1243 Lana, A., Bell, T. G., Simó, R., Vallina, S. M., Ballabrera-Poy, J., Kettle, A. J., et al. (2011). An updated
 1244 climatology of surface dimethylsulfide concentrations and emission fluxes in the global ocean. *Global*
 1245 *Biogeochemical Cycles*, 25(1), n/a-n/a. <Go to ISI>://WOS:000286755000001
- 1246 Leon, D. C., Wang, Z., & Liu, D. (2008). Climatology of drizzle in marine boundary layer clouds based on 1 year of
 1247 data from CloudSat and Cloud-Aerosol Lidar and Infrared Pathfinder Satellite Observations (CALIPSO).
 1248 *Journal of Geophysical Research*, 113.
- 1249 Liu, X., Ma, P. L., Wang, H., Tilmes, S., Singh, B., Easter, R. C., et al. (2016). Description and evaluation of a new
 1250 four-mode version of the Modal Aerosol Module (MAM4) within version 5.3 of the Community
 1251 Atmosphere Model. *Geoscientific Model Development*, 9(2), 505-522. <Go to
 1252 ISI>://WOS:000376933700003
- 1253 Mauldin, R. L., Tanner, D. J., Heath, J. A., Huebert, B. J., & Eisele, F. L. (1999). Observations of H₂SO₄ and MSA
 1254 during PEM-Tropics-A. *Journal of Geophysical Research: Atmospheres*, 104(D5), 5801-5816.
- 1255 McCoy, D. T., Burrows, S. M., Wood, R., Grosvenor, D. P., Elliott, S. M., Ma, P. L., et al. (2015). Natural aerosols
 1256 explain seasonal and spatial patterns of Southern Ocean cloud albedo. *Sci Adv*, 1(6), e1500157.
 1257 <https://www.ncbi.nlm.nih.gov/pubmed/26601216>
- 1258 McCoy, I. L., Bretherton, C. S., Wood, R., Twohy, C. H., Gettelman, A., Bardeen, C. G., & Toohey, D. W. (2021).
 1259 Supporting data for the manuscript: "Influences of Recent Particle Formation on Southern Ocean Aerosol
 1260 Variability and Low Cloud Properties" (Publication no. doi:10.5281/zenodo.4480387).
- 1261 McCoy, I. L., McCoy, D. T., Wood, R., Regayre, L., Watson-Parris, D., Grosvenor, D. P., et al. (2020). The
 1262 hemispheric contrast in cloud microphysical properties constrains aerosol forcing. *Proc Natl Acad Sci U S*
 1263 *A*, 117(32), 18998-19006. <https://www.ncbi.nlm.nih.gov/pubmed/32719114>
- 1264 McFarquhar, G. M., Bretherton, C., Marchand, R., Protat, A., DeMott, P. J., Alexander, S. P., et al. (2020).
 1265 Observations of clouds, aerosols, precipitation, and surface radiation over the Southern Ocean: An
 1266 overview of CAPRICORN, MARCUS, MICRE and SOCRATES. *Bulletin of the American Meteorological*
 1267 *Society*, 1-92. <https://journals.ametsoc.org/view/journals/bams/aop/BAMS-D-20-0132.1/BAMS-D-20-0132.1.xml>
 1268
- 1269 Modini, R. L., Frossard, A. A., Ahlm, L., Russell, L. M., Corrigan, C. E., Roberts, G. C., et al. (2015). Primary
 1270 marine aerosol-cloud interactions off the coast of California. *Journal of Geophysical Research:*
 1271 *Atmospheres*, 120(9), 4282-4303.
- 1272 Mulcahy, J. P., Jones, C., Sellar, A., Johnson, B., Boutle, I. A., Jones, A., et al. (2018). Improved Aerosol Processes
 1273 and Effective Radiative Forcing in HadGEM3 and UKESM1. *Journal of Advances in Modeling Earth*
 1274 *Systems*, 10(11), 2786-2805. <Go to ISI>://WOS:000452864500007
- 1275 Noone, K. J., Ogren, J. A., Heintzenberg, J., Charlson, R. J., & Covert, D. S. (1988). Design and Calibration of a
 1276 Counterflow Virtual Impactor for Sampling of Atmospheric Fog and Cloud Droplets. *Aerosol Science and*
 1277 *Technology*, 8(3), 235-244. <Go to ISI>://WOS:A1988N998900004
- 1278 O, K.-T., Wood, R., & Bretherton, C. S. (2018). Ultraclean Layers and Optically Thin Clouds in the Stratocumulus-
 1279 to-Cumulus Transition. Part II: Depletion of Cloud Droplets and Cloud Condensation Nuclei through
 1280 Collision-Coalescence. *Journal of the Atmospheric Sciences*, 75(5), 1653-1673. <Go to
 1281 ISI>://WOS:000434270600017
- 1282 O'Dowd, C. D., Langmann, B., Varghese, S., Scannell, C., Ceburnis, D., & Facchini, M. C. (2008). A combined
 1283 organic-inorganic sea-spray source function. *Geophysical Research Letters*, 35(1). <Go to
 1284 ISI>://WOS:000252182900001

- 1285 O'Dowd, C. D., Smith, M. H., Consterdine, I. E., & Lowe, J. A. (1997). Marine aerosol, sea-salt, and the marine
 1286 sulphur cycle: A short review. *Atmospheric Environment*, 31(1), 73-80. Article. <Go to
 1287 ISI>://WOS:A1997VP27300007
- 1288 Orsini, D. A., Wiedensohler, A., Stratmann, F., & Covert, D. S. (1999). A New Volatility Tandem Differential
 1289 Mobility Analyzer to Measure the Volatile Sulfuric Acid Aerosol Fraction. *Journal of Atmospheric and
 1290 Oceanic Technology*, 16(6), 760-772. <Go to ISI>://WOS:000080802600011
- 1291 Prather, K. A., Bertram, T. H., Grassian, V. H., Deane, G. B., Stokes, M. D., Demott, P. J., et al. (2013). Bringing
 1292 the ocean into the laboratory to probe the chemical complexity of sea spray aerosol. *Proc Natl Acad Sci U S
 1293 A*, 110(19), 7550-7555. <https://www.ncbi.nlm.nih.gov/pubmed/23620519>
- 1294 Quinn, P. K., & Bates, T. S. (2011). The case against climate regulation via oceanic phytoplankton sulphur
 1295 emissions. *Nature*, 480(7375), 51-56. <https://www.ncbi.nlm.nih.gov/pubmed/22129724>
- 1296 Quinn, P. K., Coffman, D. J., Johnson, J. E., Upchurch, L. M., & Bates, T. S. (2017). Small fraction of marine cloud
 1297 condensation nuclei made up of sea spray aerosol. *Nature Geoscience*, 10(9), 674-679. <Go to
 1298 ISI>://WOS:000409229600015
- 1299 Quinn, P. K., Collins, D. B., Grassian, V. H., Prather, K. A., & Bates, T. S. (2015). Chemistry and related properties
 1300 of freshly emitted sea spray aerosol. *Chem Rev*, 115(10), 4383-4399.
 1301 <https://www.ncbi.nlm.nih.gov/pubmed/25844487>
- 1302 Raes, F. (1995). Entrainment of free tropospheric aerosols as a regulating mechanism for cloud condensation nuclei
 1303 in the remote marine boundary layer. *Journal of Geophysical Research*, 100(D2), 2893-2903. <Go to
 1304 ISI>://WOS:A1995QJ63000013
 1305 [http://onlinelibrary.wiley.com/store/10.1029/94JD02832/asset/jgrd3417.pdf?v=1&t=i19ui59c&s=0fb373f7ac4989db](http://onlinelibrary.wiley.com/store/10.1029/94JD02832/asset/jgrd3417.pdf?v=1&t=i19ui59c&s=0fb373f7ac4989db34b73c4947cc688497f2fda4)
 1306 [34b73c4947cc688497f2fda4](http://onlinelibrary.wiley.com/store/10.1029/94JD02832/asset/jgrd3417.pdf?v=1&t=i19ui59c&s=0fb373f7ac4989db34b73c4947cc688497f2fda4)
- 1307 Regayre, L. A., Schmale, J., Johnson, J. S., Tatzelt, C., Baccharini, A., Henning, S., et al. (2019). The value of remote
 1308 marine aerosol measurements for constraining radiative forcing uncertainty. *Atmos. Chem. Phys. Discuss.*,
 1309 2019, 1-11. <https://www.atmos-chem-phys-discuss.net/acp-2019-1085/>
- 1310 Revell, L. E., Kremser, S., Hartery, S., Harvey, M., Mulcahy, J. P., Williams, J., et al. (2019). The sensitivity of
 1311 Southern Ocean aerosols and cloud microphysics to sea spray and sulfate aerosol production in the
 1312 HadGEM3-GA7.1 chemistry–climate model. *Atmospheric Chemistry and Physics*, 19(24), 15447-15466.
 1313 <Go to ISI>://WOS:000503444400006
- 1314 Saliba, G., Sanchez, K. J., Russell, L. M., Twohy, C. H., Roberts, G. C., Lewis, S., et al. (2020). Organic
 1315 composition of three different size ranges of aerosol particles over the Southern Ocean. *Aerosol Science
 1316 and Technology*, 55(3), 268-288. <https://doi.org/10.1080/02786826.2020.1845296>
- 1317 Sanchez, K. J., Chen, C. L., Russell, L. M., Betha, R., Liu, J., Price, D. J., et al. (2018). Substantial Seasonal
 1318 Contribution of Observed Biogenic Sulfate Particles to Cloud Condensation Nuclei. *Scientific Reports*,
 1319 8(1), 3235. <https://www.ncbi.nlm.nih.gov/pubmed/29459666>
- 1320 Sanchez, K. J., & Roberts, G. (2018). *SOCRATES CCN measurements*.
- 1321 Sanchez, K. J., Roberts, G. C., Saliba, G., Russell, L. M., Twohy, C., Reeves, M. J., et al. (2021). Measurement
 1322 report: Cloud processes and the transport of biological emissions affect southern ocean particle and cloud
 1323 condensation nuclei concentrations. *Atmospheric Chemistry and Physics*, 21(5), 3427-3446.
- 1324 Schmale, J., Baccharini, A., Thurnherr, I., Henning, S., Efraim, A., Regayre, L., et al. (2019). Overview of the
 1325 Antarctic Circumnavigation Expedition: Study of Preindustrial-like Aerosols and Their Climate Effects

- 1326 (ACE-SPACE). *Bulletin of the American Meteorological Society*, 100(11), 2260-2283.
 1327 <https://journals.ametsoc.org/doi/abs/10.1175/BAMS-D-18-0187.1>
- 1328 Schmid, O., Eimer, B., Hagen, D. E., & Whitefield, P. D. (2002). Investigation of Volatility Method for Measuring
 1329 Aqueous Sulfuric Acid on Mixed Aerosols. *Aerosol Science and Technology*, 36(8), 877-889. <Go to
 1330 ISI>://WOS:000176493400003
- 1331 Seinfeld, J. H., & Pandis, S. N. (2016). *Atmospheric Chemistry and Physics : From Air Pollution to Climate*
 1332 *Change*. New York, UNITED STATES: John Wiley & Sons, Incorporated.
- 1333 Stein, A. F., Draxler, R. R., Rolph, G. D., Stunder, B. J. B., Cohen, M. D., & Ngan, F. (2015). NOAA's HYSPLIT
 1334 Atmospheric Transport and Dispersion Modeling System. *Bulletin of the American Meteorological Society*,
 1335 96(12), 2059-2077. <Go to ISI>://WOS:000368500900001
- 1336 Stephens, G. L., L'Ecuyer, T., Forbes, R., Gettelmen, A., Golaz, J.-C., Bodas-Salcedo, A., et al. (2010). Dreary state
 1337 of precipitation in global models. *Journal of Geophysical Research: Atmospheres*, 115(D24). <Go to
 1338 ISI>://WOS:000285642000008
- 1339 Twohy, C. H., Anderson, J. R., Toohey, D. W., Andrejczuk, M., Adams, A., Lytle, M., et al. (2013). Impacts of
 1340 aerosol particles on the microphysical and radiative properties of stratocumulus clouds over the southeast
 1341 Pacific Ocean. *Atmospheric Chemistry and Physics*, 13(5), 2541-2562. <Go to
 1342 ISI>://WOS:000316960500016
- 1343 Twohy, C. H., Clement, C. F., Gandrud, B. W., Weinheimer, A. J., Campos, T. L., Baumgardner, D., et al. (2002).
 1344 Deep convection as a source of new particles in the midlatitude upper troposphere. *Journal of Geophysical*
 1345 *Research: Atmospheres*, 107(D21), AAC 6-1-AAC 6-10. <Go to ISI>://WOS:000180860300012
- 1346 Twohy, C. H., DeMott, P. J., Russell, L. M., Toohey, D. W., Rainwater, B., Geiss, R., et al. (2021). Cloud-
 1347 Nucleating Particles over the Southern Ocean in a Changing Climate. *Earth's Future*, n/a(n/a),
 1348 e2020EF001673. <https://agupubs.onlinelibrary.wiley.com/doi/abs/10.1029/2020EF001673>
- 1349 Twohy, C. H., Schanot, A. J., & Cooper, W. A. (1997). Measurement of Condensed Water Content in Liquid and Ice
 1350 Clouds Using an Airborne Counterflow Virtual Impactor. *Journal of Atmospheric and Oceanic*
 1351 *Technology*, 14(1), 197-202. <Go to ISI>://WOS:A1997WD27300015
- 1352 Twomey, S. (1977). The Influence of Pollution on the Shortwave Albedo of Clouds. *Journal of the Atmospheric*
 1353 *Sciences*, 34(7), 1149-1152. Note. <Go to ISI>://WOS:A1977DP78800020
 1354 <http://journals.ametsoc.org/doi/pdf/10.1175/1520-0469%281977%29034%3C1149%3ATIOPOT%3E2.0.CO%3B2>
- 1355 UCAR/NCAR, E. O. L. (2017). *Low Rate (LRT - 1 sps) Navigation, State Parameter, and Microphysics Flight-*
 1356 *Level Data (Version 1.2)*.
- 1357 UCAR/NCAR, E. O. L. (2019). *Low Rate (LRT - 1 sps) Navigation, State Parameter, and Microphysics Flight-*
 1358 *Level Data (Version 1.3)*.
- 1359 Weber, R. J., Chen, G., Davis, D. D., Mauldin, R. L., Tanner, D. J., Eisele, F. L., et al. (2001). Measurements of
 1360 enhanced H₂SO₄ and 3-4 nm particles near a frontal cloud during the First Aerosol Characterization
 1361 Experiment (ACE 1). *Journal of Geophysical Research: Atmospheres*, 106(D20), 24107-24117. <Go to
 1362 ISI>://WOS:000171974000015
- 1363 Williams, K. D., Bodas-Salcedo, A., Déqué, M., Fermepin, S., Medeiros, B., Watanabe, M., et al. (2013). The
 1364 Transpose-AMIP II Experiment and Its Application to the Understanding of Southern Ocean Cloud Biases
 1365 in Climate Models. *Journal of Climate*, 26(10), 3258-3274. <Go to ISI>://WOS:000318775900016

- 1366 Williamson, C. J., Kupc, A., Axisa, D., Bilsback, K. R., Bui, T., Campuzano-Jost, P., et al. (2019). A large source of
1367 cloud condensation nuclei from new particle formation in the tropics. *Nature*, 574(7778), 399-403.
1368 <https://www.ncbi.nlm.nih.gov/pubmed/31619794>
- 1369 Wood, R., Leon, D., Lebsock, M., Snider, J., & Clarke, A. D. (2012). Precipitation driving of droplet concentration
1370 variability in marine low clouds. *Journal of Geophysical Research: Atmospheres*, 117(D19), n/a-n/a.
- 1371 Wood, R., O, K.-T., Bretherton, C. S., Mohrmann, J., Albrecht, B. A., Zuidema, P., et al. (2018). Ultraclean Layers
1372 and Optically Thin Clouds in the Stratocumulus-to-Cumulus Transition. Part I: Observations. *Journal of the*
1373 *Atmospheric Sciences*, 75(5), 1631-1652. <Go to ISI>://WOS:000434270600016
- 1374 Zender, C. (2001). Particle Size Distributions: Theory and Application to Aerosols, Clouds, and Soils.
- 1375 Zheng, G., Kuang, C., Uin, J., Watson, T., & Wang, J. (2020). Large contribution of organics to condensational
1376 growth and formation of cloud condensation nuclei (CCN) in the remote marine boundary layer.
1377 *Atmospheric Chemistry and Physics*, 20(21), 12515-12525.
- 1378 Zheng, G., Wang, Y., Aiken, A. C., Gallo, F., Jensen, M. P., Kollias, P., et al. (2018). Marine boundary layer aerosol
1379 in the eastern North Atlantic: seasonal variations and key controlling processes. *Atmospheric Chemistry*
1380 *and Physics*, 18(23), 17615-17635. <Go to ISI>://WOS:000452860300004
- 1381 Zhou, X., Atlas, R., McCoy, I. L., Bretherton, C. S., Bardeen, C., Gettelman, A., et al. (2020). Evaluation of cloud
1382 and precipitation simulations in CAM6 and AM4 using observations over the Southern Ocean. *Earth and*
1383 *Space Science*.
1384